Journal of Materials Science: Materials in Electronics (2019) 30:11888–11906
https://doi.org/10.1007/s10854-019-01522-7

Enhancement of electrical conductivity and magnetic properties of bimetallic Schiff base complex on grafting to MWCNTs

Rashmi Gupta[1] · **Bachcha Singh**[1]

Received: 30 December 2018 / Accepted: 16 May 2019 / Published online: 25 May 2019

Abstract

In present work, we report a newly synthesized nano-inorganic hybrid magnetic material, [SBCu(II)Gd(III)]@MWCNT-COOH which is obtained by anchoring of a copper(II)–gadolinium(III) heteronuclear bimetallic complex, [triaqua(2-hydroxy-1,3-bis(3-methoxysalicylaldiminato)Cu(II)Gd(III)dinitrato)]nitrate monohydrate, [SBCu(II)Gd(III)] to carboxylated multiwalled carbon nanotubes (MWCNT-COOH) through a chemical method. MWCNT-COOH have been loaded with a number of [SBCu(II)Gd(III)] molecules on their surfaces, which generated multinuclear metal centers. [SBCu(II)Gd(III)]@MWCNT-COOH was characterized by FT-IR, UV–Vis, TGA, powder XRD, Raman spectroscopy, TEM, HRSEM, EDAX and elemental mapping. The DC electrical conductivity of materials was evaluated using two probe method suggesting that [SBCu(II)Gd(III)]@MWCNT-COOH is more conducting than [SBCu(II)Gd(III)]. The increased conductivity of [SBCu(II)Gd(III)]@MWCNT-COOH is confirmed by CV and EIS study. The capacitive and dielectric properties of the materials were investigated by Mott–Schottky electrochemical analysis. The positive value of slope signified n-type semiconducting nature of materials. The lower slope for [SBCu(II)Gd(III)] signified the strong dielectric behavior of the material. The positive shift in flat-band potential of [SBCu(II)Gd(III)]@MWCNT-COOH compared to [SBCu(II)Gd(III)] indicated its more conducting nature. Further small optical band gap obtained for [SBCu(II)Gd(III)]@MWCNT-COOH than [SBCu(II)Gd(III)] by UV–Vis studies suggested better conductivity of nano-inorganic hybrid material. Field dependent magnetization revealed enhanced saturation magnetization, remanent magnetization and coercivity of [SBCu(II)Gd(III)]@MWCNT-COOH due to generation of multinuclear metal centers on carboxylated MWCNTs. The temperature dependent magnetization measurement exhibited overlapping of field cooled and zero field cooled curves in entire temperature range (2–300 K), suggests intrinsic ferromagnetism in [SBCu(II)Gd(III)]@MWCNT-COOH. Hence, trend in variation of magnetization with magnetic field and temperature opens its utility in spin-based electronic devices.

1 Introduction

Carbon nanotubes (CNTs) have remarkably high surface area, high tensile strength, large aspect ratio and unique electrical, mechanical and thermal properties [1]. CNTs are one dimensional carbon nanostructures made of sp^2-hybridized carbon atoms leading to highly delocalized π-electrons systems, hence have excellent potential to promote communication between paramagnetic centers at long distances [2]. CNTs have considerable interest in electronics and electrical applications due to its low density, low threshold voltage, large aspect ratio, high current carrying capacity, tuneable electrical properties and ballistic electron conduction properties [3]. The quantum movement of charge carries (electrons) within one dimensional structures of CNTs with negligible electrical resistivity referred as ballistic conduction property, is responsible for its better conductivity compared to metals [4, 5]. Therefore, CNTs, in particular, have generated much interest as a conducting filler and as a promising supporting material to enhance electrical conductivity of various materials, i.e., polymers [5], nanocomposites [6], nanomaterials [7] etc. With these unique structures and properties, CNTs have been used for various potential applications including nanoelectronic devices, optoelectronic devices, fuel cells, batteries, photovoltaics, semiconductor devices, displays, photonics, catalysts, sensors, drug delivery systems, molecular diodes, and magnetic storage devices [8–10]. The main obstacle which limited the potential of

✉ Bachcha Singh
bsinghbhu@rediffmail.com

[1] Department of Chemistry, Centre of Advance Study, Institute of Science, Banaras Hindu University, Varanasi 221005, India

CNTs in plethora of applications is their insolubility in any solvent. However, functionalization can improve solubility, reactivity and decrease the toxicity of CNTs and provide anchor point for applications dependent post modification with various materials [10, 11]. Two main modes used for functionalization of CNTs are exohedral (covalent and non-covalent) and endohedral (via encapsulation) [12].

Among these methods of functionalization, the covalent bond mode allows formation of more stable functionalized CNTs with modified physical and chemical properties [13]. The chemical combination of organic/inorganic materials and CNTs in order to obtain nano hybrid structures, follows mainly two strategies: (i) direct attachment of functional groups to the CNTs surface and (ii) the use of CNTs surface bound carboxylic acids as anchor point for further modification to obtain various potential applications. Under first strategy, Margrave and co-workers [14] first reported the fluorination of SWNTs at several different temperatures. However, carboxylation is commonly known approach to produce stable dispersed CNTs and subsequent derivatization of carboxylic group. The anchoring of long alkyl chains to SWNTs was first reported by Haddon and co-workers [15] via amide linkages followed by several reports on acid functionalized MWCNTs [11, 16–18]. CNTs synthesized by catalytic CVD method using catalysts, such as Fe, Ni or Co exhibit magnetic characteristics [19]. Purification of these catalysts typically utilizes the treatment of nanotubes by nitric and sulfuric acid, hence decrease in the degree of magnetization has been observed. However, some amount of Fe catalyst which is hermetically sealed either between or within the walls of CNTs remains trapped after acid treatment is responsible for magnetism in MWCNT-COOH [20, 21].

Schiff bases are one of the most widely used classes of ligands in coordination chemistry. These provide binding sites to the transition, non-transition, lanthanide and actinide metal ions to fabricate metal complexes with targeted properties. Schiff base complexes have considerable interest due to versatility and important biological, catalytic and magnetic properties [22, 23]. Some CNT-inorganic hybrid materials have been fabricated by anchoring of Schiff base metal complexes on CNTs surfaces for their catalytic [24–30] and sensing applications [31]. Salavati-Niasari et al. reported several papers related to covalent grafting of CNTs with monometallic Schiff base complexes such as [Ni((OH)$_2$-salen)], [Cu((OH)$_2$-salen)] and [Co((OH)$_2$-salen)] and Schiff base complexes of dioxomolybdenum(VI) functionalized CNTs were used as a nano-catalyst for oxidation of phenol [32], ethylbenzene [33], aliphatic and aromatic alcohols [34] and epoxidation of cyclohexene [35], respectively. BaFe$_{12}$O$_{19}$-chitosan Schiff base Ag (I) complexes embedded MWCNTs are reported as high-performance electromagnetic materials [36]. Several papers have reported preparation of magnetic CNTs [37]. Elias et al. [38] reported encapsulation of monocrystalline Fe–Co nanowire inside MWCNTs and inorganic CNT hybrid material $Mn_{12}O_{12}(O_2CCH_3)16(H_2O)_4$@GMWNT was prepared via encapsulation by Giménez-López et al. [39]. Fabrication of iron oxide nanoparticles decorated MWCNTs magnetic composites by chemical precipitation method was reported by Yong Cao [40]. Light weight PVA membrane based on CNTs doped Schiff bases and their iron complexes were found to have electromagnetic wave absorption property [41]. There is no report on heteronuclear bimetallic Schiff base complex functionalized MWCNTs.

In present work, Cu–Gd bimetallic Schiff base complex [SBCu(II)Gd(III)] has been synthesized following reported procedure [42] with slight modification. Free hydroxyl group of the synthesized bimetallic complex was used for covalent attachment of acyl chloride of MWCNTs via simple nucleophilic substitution reaction to generate multi nuclear metal centers on surface of MWCNTs. These materials have been characterized by FT-IR, UV–Vis, TGA, Powder XRD, Raman, EDAX, elemental mapping, HRSEM, TEM, CV, electrochemical impedance study, DC electrical conductivity and magnetic measurements. The enhancement in electrical conductivity and magnetic properties of Schiff base complex due to its grafting on highly conjugated MWCNT-COOH surfaces is reported.

2 Materials and methods

2.1 Materials

All the reagents and solvents used were of analytical grade and were used without any further purification. The carboxylic acid functionalized multiwalled CNTs > 8%, average diameter of 9.5 nm and length of 1.5 µm; 1,3-diamino-2-propanol, 2-Hydroxy-3-methoxybenzaldehyde (o-Vanillin), copper(II) acetate monohydrate, gadolinium(III) nitrate hexahydrate, thionyl chloride, tetrabutylammonium perchlorate and ferrocene were purchased from Sigma Aldrich Chemicals Private Limited, India. Organic solvents were obtained from SD fine chemicals, India. Potassium ferrocyanide, potassium ferricyanide and Potassium chloride were supplied by Qualigens (Mumbai, India).

2.2 Synthesis

2.2.1 Synthesis of monometallic complex [SBCu(II)]

The complex has been prepared in situ using the method [42]. 2-Hydroxy-3-methoxy benzaldehyde (0.304 g, 2 mmol) was dissolved in 10 mL dry methanol. To this a solution of 1, 3-diamino-2-propanol (0.09 g, 1 mmol) dissolved in dry methanol (5 mL) was added. The reaction mixture was allowed to reflux at 60 °C on oil bath for 1 h with stirring. After cooling the reaction mixture to room temperature triethylamine (0.42 ml, 3 mmol) was added followed by addition of 5 mL methanol solution of copper acetate monohydrate [$Cu(CH_3COO)_2 \cdot H_2O$] [(0.20 g, 1 mmol)]. Reaction mixture was again refluxed at 60 °C for 5 h. A light green precipitate appeared which was separated by filtration and washed with methanol then dried in vacuum over anhydrous $CaCl_2$, yield 0.371 g (84%).

2.2.2 Synthesis of bimetallic complex [SBCu(II)Gd(III)]

Schiff base complex, [SBCu(II)] (0.22 g, 0.5 mmol) was dissolved in dry acetonitrile (15 mL) by heating. To this gadolinium nitrate hexahydrate, $Gd^{III}(NO_3)_3 \cdot 6H_2O$ (0.226 g, 0.5 mmol) dissolved in dry methanol (5 mL) was added drop wise and reaction mixture was refluxed at 76 °C on oil bath for 6 h with stirring. Evaporation of the solution under reduced pressure yielded green viscous mass, which was triturated with THF several times to get complex in powder form. The complex was filtered, washed with THF followed by acetonitrile several times and dried under vacuum, yield 0.304 g (73%).

2.2.3 Synthesis of MWCNT-COCl from MWCNT-COOH

MWCNT-COOH (0.05 g) was taken in dry DMF (50 mL) and sonicated for 1 h at 40–45 °C. After sonication, 25 mL of thionyl chloride was added slowly in drops. Reaction mixture was heated at 120 °C on oil bath for 24 h with continuous stirring. Excess of $SOCl_2$ was distilled out and allowed to cool at room temperature.

2.2.4 Synthesis of [SBCu(II)Gd(III)]@MWCNT-COOH

To the above suspension of MWCNT-COCl, pyridine (1 mL) was added followed by [SBCu(II)Gd(III)] (0.20 g) in 10 mL dry DMF slowly. The reaction mixture was sonicated for 1 h at 40–45 °C and heated at 120 °C on oil bath with continuous stirring for 96 h. The resulting product was washed several times thoroughly via centrifugation at 12000 rpm for 40–45 min with DMF, THF and finally with methanol. The product was dried under vacuum. The synthetic route for preparation of nano-inorganic hybrid material is shown in Scheme 1.

2.2.5 Preparation of electrode for electrochemical measurement

The surface of the glassy carbon (GC) electrode was cleaned by rubbing it over Buehler-felt pad using alumina powder and then it was sonicated for 5 min in triple distilled water and allowed to dry at room temperature. To prepare the electrode, 0.1 wt% suspension of the materials was prepared in 1 mL DMF and was sonicated for 30 min. After sonication, 10 µL of the suspension was coated on the clean GC electrode surface and was left to dry at room temperature. Further, these electrodes were used for CV and electrochemical impedance study.

2.3 Techniques

FT-IR spectra were recorded on PerkinElmer spectrophotometer using KBr pellets over the range of 4000–400 cm^{-1}. The electronic spectra of all compounds were obtained by UV 1700 Pharma Spec, Shimadzu spectrophotometer. Thermogravimetric analysis (TGA) was carried out under nitrogen atmosphere on Perkin Elmer-STA 6000 instrument with a flow rate of 20.0 ml min^{-1} and heating rate at 10 °C min^{-1}. Powder X-ray diffraction (XRD) patterns were obtained by Bruker D8 Advance X-ray diffractometer using Cu-Kα radiation (0.1541 nm). Raman spectra were recorded on Renishaw micro-Raman spectrometer at 532 nm solid state diode laser with 0.5% intensity of 100 milliwatts. Transmission electron microscopy (TEM) images were obtained from TECNAI 20 G^2 microscope with an accelerating voltage of 200 kV. HRSEM (high resolution scanning electron microscopy) study was performed on FEI, NOVA NANOSEM 450 Scanning electron microscope coupled with EDAX spectrometer and Si(Li) detector for elemental analysis. In HRSEM analysis, to reduce charging effects of MWCNTs, a 2 nm gold coating was applied to MWCNT power sprinkled carbon adhesive tabs. The room temperature DC electrical conductivity measurement was carried out with a Keithley 2635B instrument by fabricating a double probe conductivity bridge cell. Electrochemical experiments were conducted by CHI-660C (USA) work station by using a conventional three-electrode system in which a cleaned glassy carbon (GC) electrode (area = 0.07 cm^2) was used as the working electrode while Pt wire was used as a counter electrode. Saturated calomel electrode (SCE) i.e. $Hg/Hg_2Cl_2/KCl(sat.)$ and Ag/AgCl electrode were used as a reference electrode for aqueous and non-aqueous electrochemical analysis, respectively. The field dependent magnetization of samples was measured by vibrating sample magnetometer (Microsense, LLC: EZ9 VSM) and temperature dependent magnetization was determined by SQUID based magnetometer (Quantum Design, MPMS-3).

3 Results and discussion

3.1 FT-IR study

FT-IR spectra for MWCNT-COOH, [SBCu(II)], [SBCu(II)Gd(III)] and [SBCu(II)Gd(III)]@MWCNT-COOH are

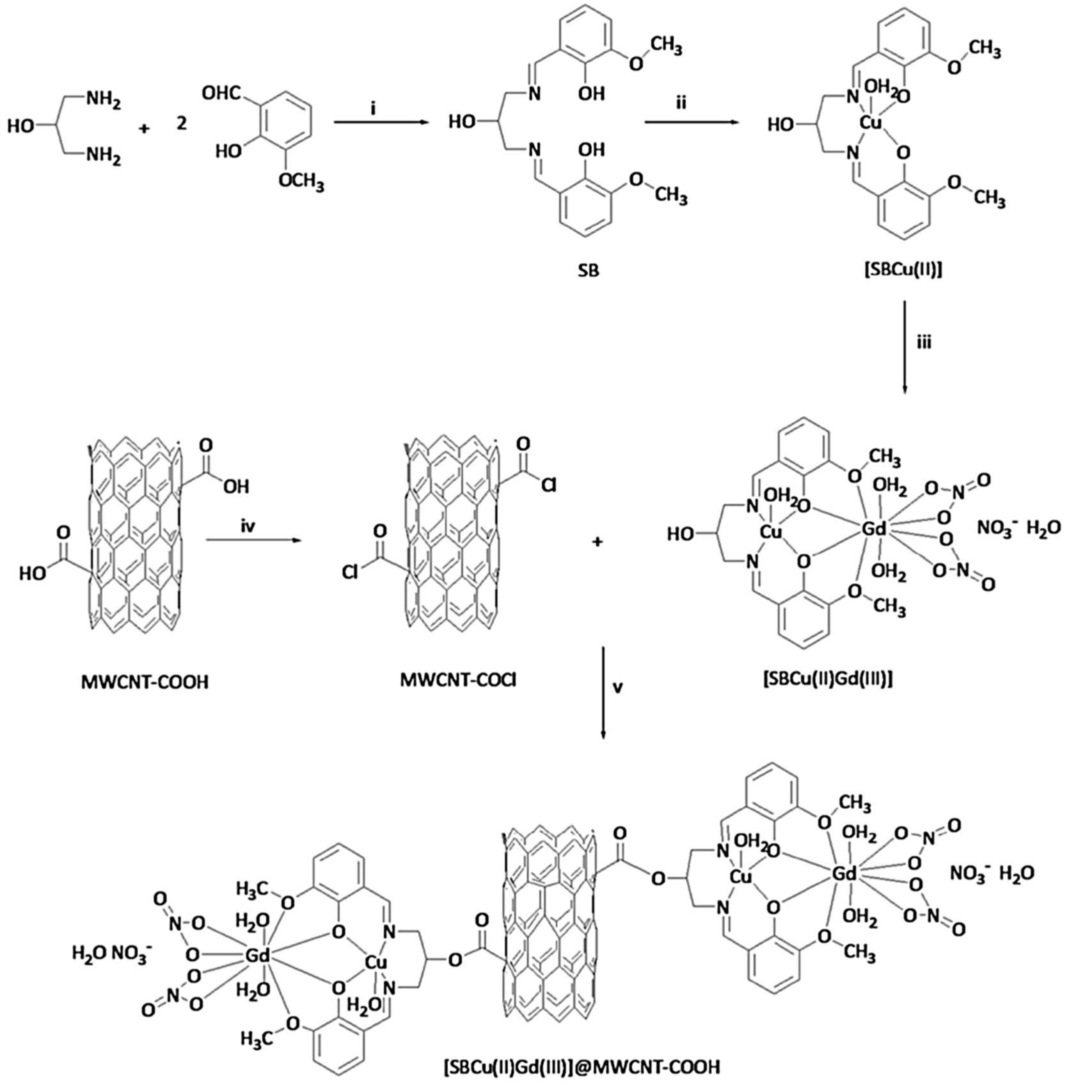

Scheme 1 Routes for the synthesis of nano-inorganic hybrid material, [SBCu(II)Gd(III)]@MWCNT-COOH and reagents: (i) MeOH (dry), (ii) NEt_3,$Cu(OAc)_2.H_2O$, (iii) $Gd(NO_3)_3·6H_2O$, (iv) Thionyl chloride, DMF(dry) and (v) Pyridine, DMF(dry)

shown in Fig. 1 and characteristic absorption bands (cm^{-1}) with assignment are given in Table 1. The FT-IR spectrum of monometallic complex [SBCu(II)] exhibited a sharp peak at around 1623 cm^{-1}, attributed to characteristic azomethine (–C=N) group of Schiff base bonded to Cu(II). The ν(C=N) band of [SBCu(II)] shifted to 1628 cm^{-1} in the spectrum of [SBCu(II)Gd(III)] [42] due to structural changes because of chelating nature of azomethine nitrogen and presence of nitrate ion bonded to Gd(III). It has been found that on covalent grafting of [SBCu(II)Gd(III)] complex to MWCNT-COOH, the ν(C=N) band shifted to higher wave number and observed at around 1639 cm^{-1} with comparatively weak intensity of band due to low concentration of [SBCu(II)Gd(III)] complex on MWCNTs surface. In case of MWCNT-COOH and [SBCu(II)Gd(III)]@MWCNT-COOH, a very weak band observed at 1742 and 1743 cm^{-1} is attributed to ν(C=O) of carbonyl group of acid and ester, respectively. In MWCNT-COOH, a peak is observed at around 3424 cm^{-1} attributed to ν(O–H) of carboxyl group [38]. The bands at 3464 and 3255 in the spectrum of [SBCu(II)] and a broad band at 3300 cm^{-1} in that of [SBCu(II)Gd(III)] are attributed to ν(O–H) of H_2O and aliphatic –OH stretching vibrations. Absence of ν(O–H) of aliphatic –OH band from spectrum of [SBCu(II)Gd(III)]@MWCNT-COOH indicated the successfully attachment of [SBCu(II)Gd(III)] complex to MWCNT-COOH.

3.2 UV–Vis spectral study

The UV–Vis spectra of the complexes [SBCu(II)] in acetonitrile and that of [SBCu(II)Gd(III)], MWCNT-COOH and [SBCu(II)Gd(III)]@MWCNT-COOH were recorded in

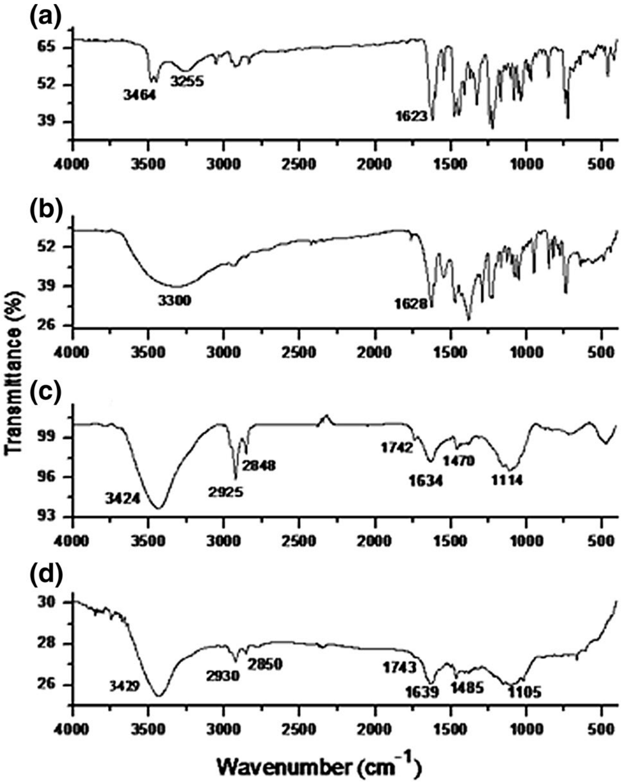

Fig. 1 FT-IR Spectra of **a** [SBCu(II)], **b** [SBCu(II)Gd(III)], **c** MWCNT-COOH and **d** [SBCu(II)Gd(III)]@MWCNT-COOH

solid state (Nujol mull) and in MeOH & DMF solutions. As shown in Fig. 2a, the spectrum of [SBCu(II)] exhibited bands at 232, 280 and 368 nm attributed to $\pi\rightarrow\pi^*$ transition of the aromatic ring [43, 44]. A broad band observed at 609 nm due to $^2B_2g \leftarrow {}^2B_1g\ (dzx, dzy \rightarrow dx^2 - y^2)$ transition of copper (II) is commensurate with square pyramidal geometry around metal ion [45]. Due to distortion in geometry at copper center, the d–d band shifted to higher wavelength at 645 nm in the complex [SBCu(II)Gd(III)]. The transitions due to gadolinium (III) in the complex [SBCu(II)Gd(III)] overlapped with charge transfer/intraligand transitions and therefore could not be identified [44]. In the spectrum Fig. 2b of [SBCu(II)Gd(III)]@MWCNT-COOH in methanol solution no absorption bands characteristic of Cu(II) and Gd(III) have been observed because of low loading of [SBCu(II)Gd(III)]. However in solid state spectrum a large number of bands are observed, which are assigned to the transitions due to $\pi\rightarrow\pi^*$, $n\rightarrow\pi^*$ and Gd(III), while the spectrum of MWCNT-COOH has a broad band due to overlapping of transitions due to $\pi\rightarrow\pi^*$ and $n\rightarrow\pi^*$.

In order to study the effect of polarity of solvent on optical properties of [SBCu(II)Gd(III)], MWCNT-COOH and [SBCu(II)Gd(III)]@MWCNT-COOH, the UV–Vis spectra were also recorded in DMF solution Fig. 2c–e. The maxima of absorption peaks shifted to higher wavelength in DMF solution compared to MeOH solution due to the less polarity and more Lewis base character of DMF [46]. Further, the red shift is observed in absorption peaks in solid state spectra compared to that in DMF solution (Fig. 2c) due to increase in intramolecular interaction and aggregation [47].

3.3 Thermogravimetric analysis

Thermal behavior of Schiff base metal complexes and their quantification on MWCNTs surfaces was investigated by TGA. Figure 3 shows TGA curves of [SBCu(II)], [SBCu(II)Gd(III)], MWCNT-COOH and [SBCu(II)Gd(III)]@MWCNT-COOH. The weight loss was observed from 30 to 900 °C at heating rate 10 °C min^{-1} under nitrogen atmosphere. The TGA data of all the compounds are summarized in Table 2. Thermogram of [SBCu(II)] showed total weight loss of 65.46% at three stages leaving behind a residue of 34.54% which is attributed to formation of CuO and some undecomposed organic moiety. The complex [SBCu(II)Gd(III)] showed 1.98% loss due to removal of one lattice H_2O molecule, 21.83% loss due to removal of $C_9H_{11}NO$ and two coordinated H_2O molecules. Further a weight loss of 38.19% corresponds to removal of $C_{10}H_{11}NO_2$, 2 NO_3^- and H_2O. The residue (37.46%) corresponds to the formation of CuO and $GdONO_3$. The weight loss found in both the complexes showed good agreement with the loss of different fragments. The TGA results showed that carboxylic acid functionalized MWCNTs are thermally very stable. This showed 21.58% weight loss in the 315–640 °C temperature range corresponding to removal of carboxylic acid group of MWCNT-COOH [24]. By comparing the thermogram of [SBCu(II)Gd(III)]@MWCNT-COOH with [SBCu(II)Gd(III)], it has been observed that in [SBCu(II)Gd(III)]@MWCNT-COOH the weight loss of 15% in the temperature range 120–255 °C may be attributed to the loss of some

Table 1 Significant FT-IR spectral bands for **a** [SBCu(II)], **b** [SBCu(II)Gd(III)], **c** MWCNT-COOH and **d** [SBCu(II)Gd(III)]@ MWCNT-COOH

Compound	ν_{OH}	ν_{CH}	$\nu_{C=O}$	$\nu_{C=N}$	$\nu_{C=C}$	Phenolic $\nu_{C–O}$	Alcohlic $\nu_{C–O}$	Acidic $\nu_{C–O}$
(a)	3255	2923	–	1623	1450	1245, 1224	1082	–
(b)	3300	2927	–	1628	1471	1294, 1238	1083	–
(c)	3424	2925	1742	–	1470–1628	–	–	1114
(d)	3429	2930	1743	1639	1485	1217	1024	1105

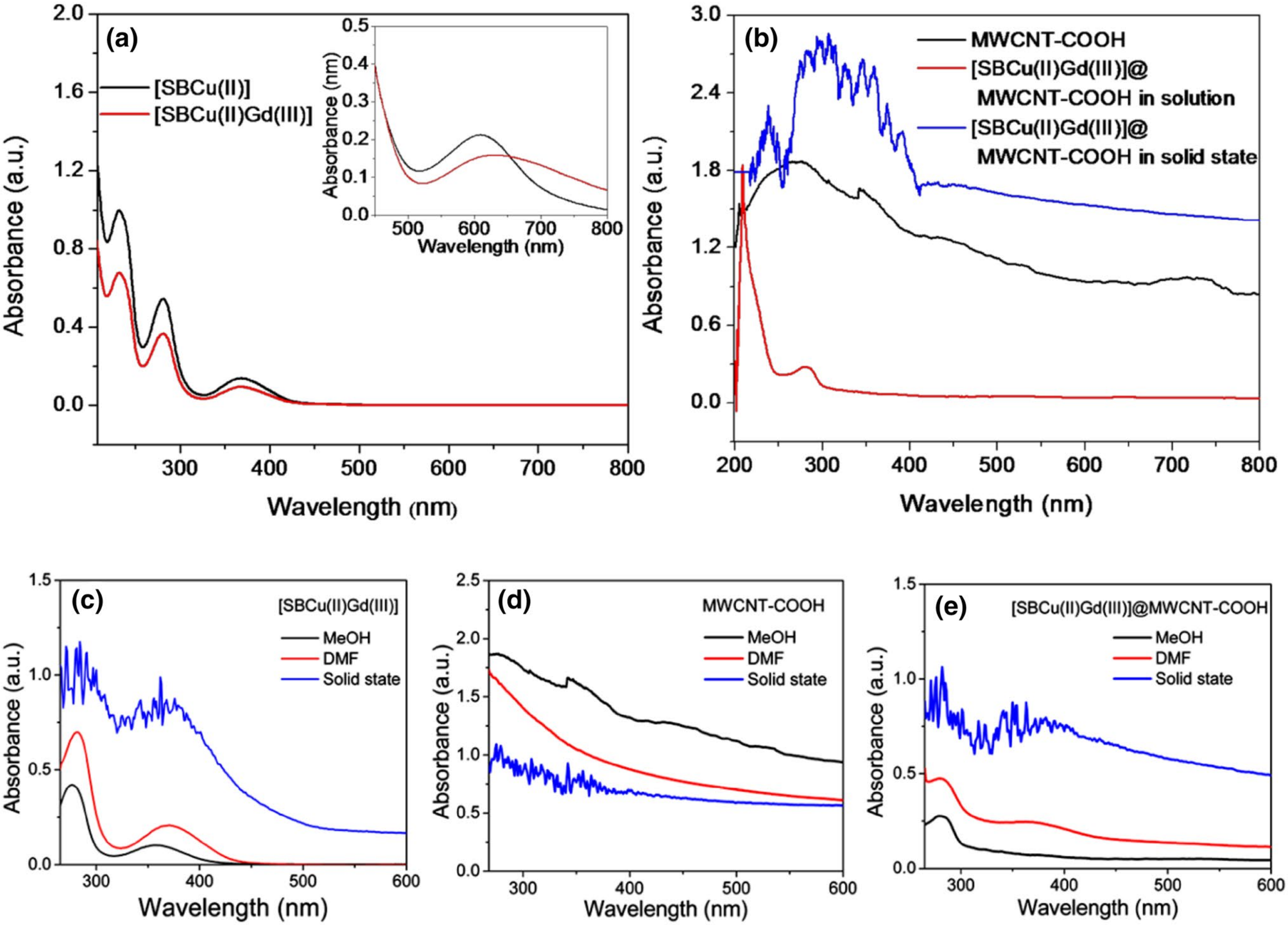

Fig. 2 UV–Vis spectra of **a** [SBCu(II)] and [SBCu(II)Gd(III)], **b** MWCNT-COOH, [SBCu(II)Gd(III)]@MWCNT-COOH in MeOH solution and [SBCu(II)Gd(III)]@MWCNT-COOH in solid state, **c** [SBCu(II)Gd(III)], **d** MWCNT-COOH and **e** [SBCu(II)Gd(III)]@ MWCNT-COOH in MeOH, DMF solution and in solid state, respectively

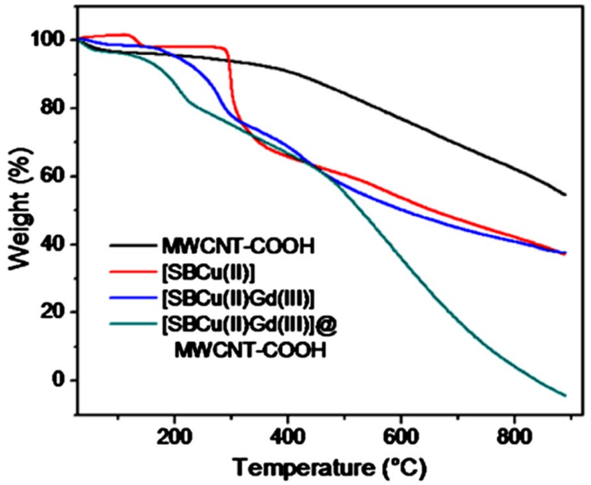

Fig. 3 TGA thermograms of [SBCu(II)], [SBCu(II)Gd(III)], MWCNT-COOH and [SBCu(II)Gd(III)]@MWCNT-COOH]

organic moiety of Schiff base molecule and weight loss of 14.59% in the temperature range 255–410 °C may be assigned to the decomposition of remaining organic moiety. The weight loss of 57.24% in the temperature range 410–900 °C may be due to decomposition of amorphous carbon as well as CNTs, as decomposition of CNTs starts around 700 °C [30]. Hence TGA study revealed that bimetallic Schiff base complex had been successfully functionalized on MWCNT-COOH surfaces and anchoring of the complex does not affect the thermal stability of MWCNTs [26].

3.4 Powder XRD study

The powder X-ray diffraction patterns of [SBCu(II)], [SBCu(II)Gd(III)], MWCNT-COOH and [SBCu(II) Gd(III)]@MWCNT-COOH are shown in Fig. 4. The powder XRD pattern of the complex [SBCu(II)] showed intense sharp peaks characteristic of the crystalline nature [48, 49]. XRD pattern of [SBCu(II)] is similar to that of Cu(II)

Table 2 TGA data of **a** [SBCu(II)], **b** [SBCu(II)Gd(III)], **c** MWCNT-COOH and **d** [SBCu(II)Gd(III)]@MWCNT-COOH]

Compound	Stage	Temp. range (°C)	Weight loss (%)		Loss of moiety	Residue
			Found	Calcd.		
(a)	I	30–144	4.78	4.1	Moisture and H_2O	$C_{19}H_{20}N_2O_5Cu$
	II	288–448	34.02	34.25	$C_9H_{11}NO$	$C_{10}H_9NO_4Cu$
	III	448–900	24.66	24.66	C_7H_8O	$C_3H_1NO_3Cu$
(b)	I	41–92	1.98	2.15	H_2O (lattice)	$C_{19}H_{26}N_5O_{17}CuGd$
	II	125–310	21.83	22.26	$C_9H_{11}NO + 2H_2O$	$C_{10}H_{11}N_4O_{14}CuGd$
	III	324–900	38.19	38.79	$C_{10}H_{11}NO_2 + 2NO_3 + H_2O$	$CuO + GdONO_3$
(c)	I	30–82	5.19	–	Moisture	–
	II	315–640	21.58	–	Carboxylic acid group (–COOH) of MWCNTs	–
	III	640–900	17.73		Decomposition of MWCNTs	–
(d)	I	33–105	4.41	–	Moisture/H_2O	–
	II	120–255	15.00	–	$C_9H_{11}NO + 2H_2O$	–
	III	255–410	14.59	–	$C_{10}H_{11}NO_2 + 2NO_3 + H_2O$	–
	IV	410–900	57.24	–	Decomposition of unreacted acid group of MWCNTs and tubical structure of MWCNTs.	–

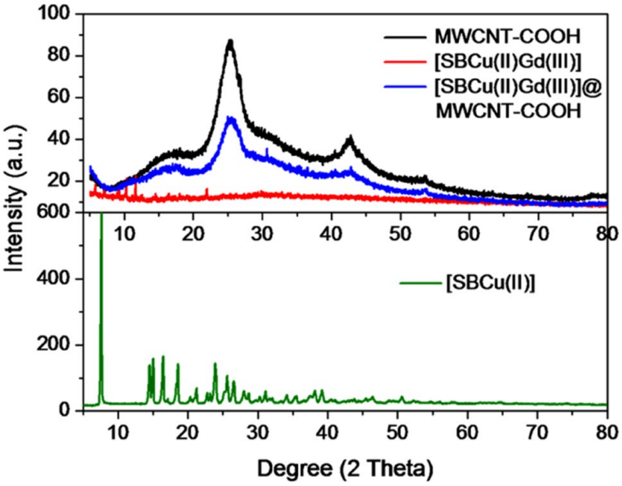

Fig. 4 Powder–XRD patterns of MWCNT-COOH, [SBCu(II)Gd(III)], [SBCu(II)Gd(III)]@MWCNT-COOH and [SBCu(II)]

complex reported by Bhaumik et al. [50] suggesting the square pyramidal geometry around Cu(II) in [SBCu(II)]. The characteristic diffraction peaks of MWCNT-COOH appeared at 25.4°, 42.8° and 53.6° corresponding to (0 0 2), (1 0 0) and (0 0 4) planes of hexagonal graphite structure [51]. These peaks appear at similar positions in [SBCu(II)Gd(III)]@MWCNT-COOH], i.e., after functionalization of MWCNT-COOH with [SBCu(II)Gd(III)]. This signifies that the crystallinity and tubular structure of the MWCNTs remains essentially preserved [30] after functionalization. XRD pattern of [SBCu(II)Gd(III)] is signature of its amorphous nature and no significant new peaks were detected when compared with the pattern of [SBCu(II)].

3.5 Raman study

Raman spectra of CNTs are reported to have characteristic G band between 1500 and 1600 cm^{-1} and D band at around 1300–1400 cm^{-1} that appear in the spectra of all graphitic structures. The characteristic *D* bands are attributed to disordered *sp*^{3} hybridized carbon atoms while *sp*^{2} hybridized carbon atoms are responsible for *G* band which originated from highly ordered sidewalls of MWCNTs. A prominent band at 2683 cm^{-1} is also exhibited by MWCNTs which is called as *G"* or *2D* band due to the overtone of the *D* band [52]. The I_D/I_G ratio depends on the number of *sp*^{3} carbon atoms present at the defect sites and the open ends; it can be used to evaluate the extent of defects in nanotubes structure [30]. Raman spectra (Fig. 5) of MWCNT-COOH exhibited *D* and *G* band at 1343 and 1578 cm^{-1} and that of [SBCu(II)Gd(III)]@MWCNT-COOH at 1346 and 1581 cm^{-1} respectively. The *2D* band appeared at 2677 and 2686 cm^{-1} for MWCNT-COOH and [SBCu(II)Gd(III)]@MWCNT-COOH respectively. On functionalization, the dispersibility of MWCNT-COOH is increased yielding less intertube interactions, hence, all the Raman bands of [SBCu(II)Gd(III)]@MWCNT-COOH are shifted to higher wave numbers compared to that of MWCNT-COOH. As a result of dispersion and debundling of nanotubes, a further up shifting is also observed in Raman bands of [SBCu(II)Gd(III)]@MWCNT-COOH compared to MWCNT-COOH [52]. The I_D/I_G ratio increased on modification of MWCNT-COOH confirming the formation of defects sites on MWCNTs surfaces on further functionalization [53].

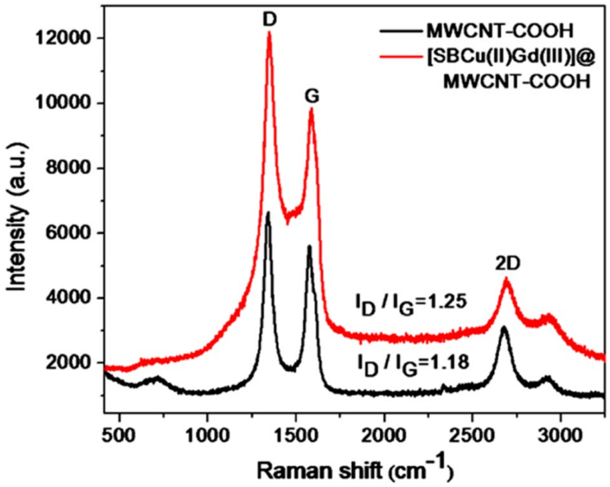

Fig. 5 Raman spectra of MWCNT-COOH and [SBCu(II)Gd(III)]@ MWCNT-COOH

3.6 TEM study

Structural study of carboxylated CNTs (MWCNT-COOH) and [SBCu(II)Gd(III)]@MWCNT-COOH, was carried out by transmission electron microscopy (TEM). From TEM images (Fig. 6a, b) of MWCNT-COOH and [SBCu(II) Gd(III)]@MWCNT-COOH, it has been found that the tubular structure as well as the length of nanotubes remained unaffected after functionalization. TEM images showed that the external average diameter of nanotubes of MWCNT-COOH and [SBCu(II)Gd(III)]@MWCNT-COOH, were approximately 12 and 26 nm under same magnification (100 nm). On comparing the TEM images of both materials, it is found that diameter of MWCNT-COOH increased by approximately 14 nm after functionalization [54].

3.7 HRSEM study

HRSEM study exhibited the morphological changes in CNTs after functionalization. From HRSEM images (Fig. 6c, e) some agglomerigation of CNTs has been found in MWCNT-COOH, which decreased in [SBCu(II) Gd(III)]@MWCNT-COOH (Fig. 6d, f) on functionalization of MWCNT-COOH with [SBCu(II)Gd(III)]. The well separation of nanotubes in [SBCu(II)Gd(III)]@ MWCNT-COOH indicated that debundling and enhancement in dispersibility of nanotubes occurred during functionalization. It is observed that the thickness of CNTs in [SBCu(II)Gd(III)]@MWCNT-COOH increased compared to MWCNT-COOH, which is also confirmed by TEM images [55]. The surface morphology of MWCNT-COOH and [SBCu(II)Gd(III)]@MWCNT-COOH is noticeably different at both magnifications (100 and 500 nm) which is attributed to uniformly attachment of heteronuclear bimetallic Schiff base complex on MWCNT-COOH surfaces resulting successful formation of [SBCu(II) Gd(III)]@MWCNT-COOH [30].

3.8 EDAX study and elemental mapping

EDAX measures surface elemental composition by determining the binding energy of electrons ejected when materials are irradiated with X-rays [30]. As shown in Fig. 7, EDAX spectra of MWCNT-COOH confirmed the presence of quantitative amount (weight and atomic percentage) of C and O elements while the presence of additional Cu, Gd and N elements is shown in [SBCu(II)Gd(III)]@ MWCNT-COOH. This confirmed the successful anchoring of SBCu(II)Gd(III)] to MWCNT-COOH. In addition to these elements, small quantity of Si, Cl and Au were also shown by EDAX spectra of [SBCu(II)Gd(III)]@MWCNT-COOH and MWCNT-COOH. The contribution of Si element is due to Si(Li) EDAX detector of HRSEM microscope [56]. The presence of elemental Cl occurred due to some unmodified acyl chloride group of MWCNT–COCl during functionalization of MWCNT-COOH with bimetallic complex. The peak due to elemental gold in EDAX spectra is observed because of gold coating of the samples for reducing the charging effect [57]. As shown in Fig. 8a, b the EDAX elemental mapping exhibited uniform distribution of all the elements over MWCNT surfaces without strong agglomeration.

3.9 DC electrical conductivity measurement

The room temperature solid state conductivity of SBCu(II) Gd(III)], MWCNT-COOH and [SBCu(II)Gd(III)]@ MWCNT-COOH were carried out using two probe method. The conductivity was determined by making the pellet of diameter (10 mm) and thickness (0.5–1.5 mm) of the materials by applying a pressure of 5 tones/cm^2 using hand operated hydraulic press. The silver paste was applied on both side of pellet to make the contact of copper wires with the conducting surfaces. The bulk resistance of the materials was calculated from the current versus voltage (I–V) characteristics (Fig. 9). The DC conductivity of materials has been calculated by using resistance and thickness of pellet. The values of resistance and conductivity are summarized in Table 3. The order of DC electrical conductivity was found to be MWCNT-COOH > [SBCu(II)Gd(III)]@ MWCNT-COOH > [SBCu(II)Gd(III)]. The increased conductivity of [SBCu(II)Gd(III)]@MWCNT-COOH compared to [SBCu(II)Gd(III)] is due to large surface area, high aspect ratio, ballistic electron conduction and highly conjugated π-electron framework of MWCNTs [3].

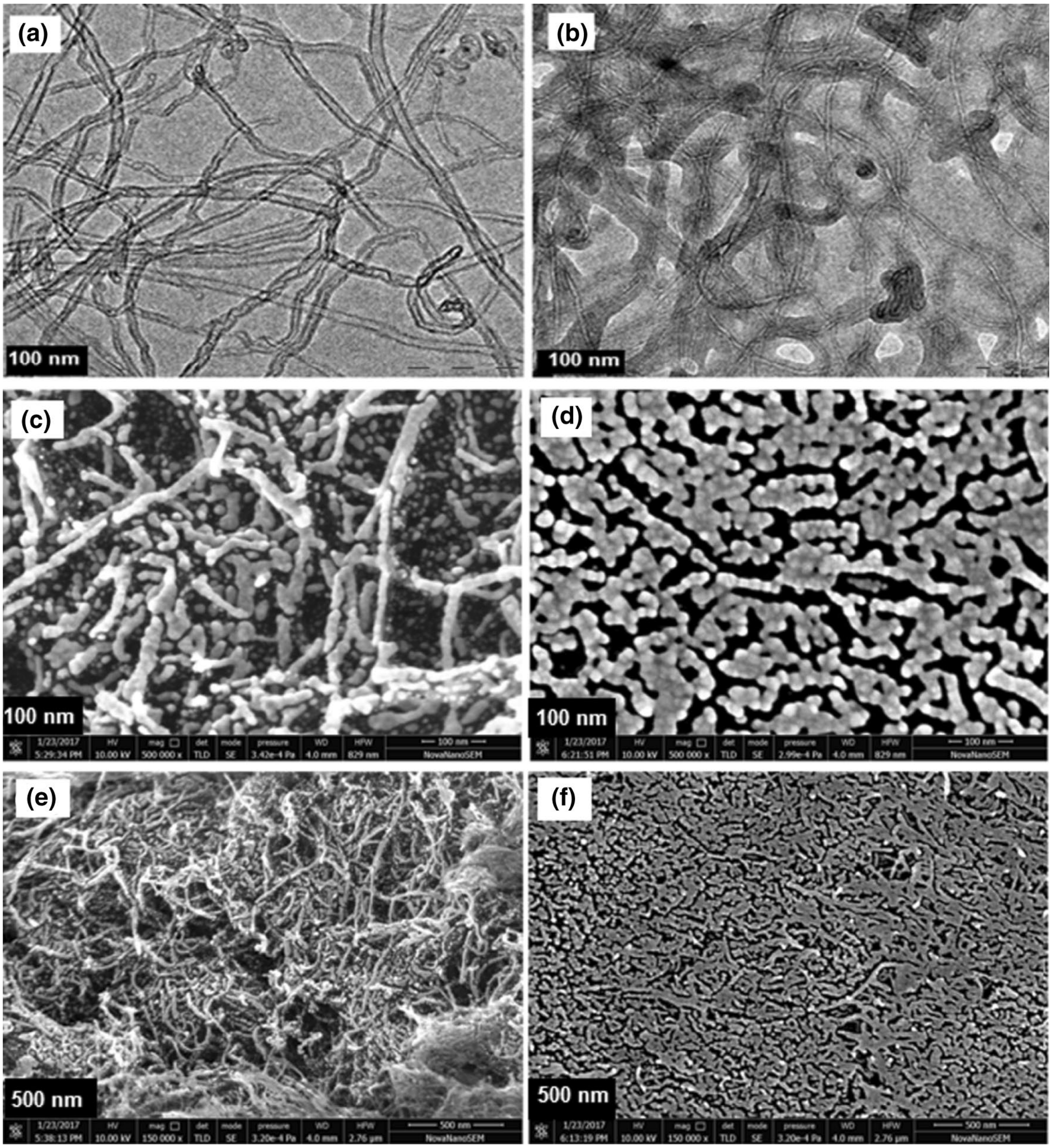

Fig. 6 TEM images of **a** MWCNT-COOH, **b** [SBCu(II)Gd(III)]@MWCNT-COOH at 100 nm magnification and HRSEM images of **c** and **e** MWCNT-COOH and **d** [SBCu(II)Gd(III)]MWCNT-COOH, at magnification 100 and 500 nm

3.10 Electrochemical behavior

3.10.1 Cyclic voltammetry

Cyclic voltammetry (CV) is a robust analytical technique that provides information related to characteristic electrochemical processes. CV is commonly employed to investigate the kinetics of redox reactions of materials, their conducting and insulating behavior [58]. All the experiments were carried out using material's drop coated glassy carbon (GC) electrodes in 2.0 mM $Fe(CN)_6^{3-}/Fe(CN)_6^{4-}$ (1:1 molar ratio) containing 0.1 M KCl. CV curves (current vs. potential) of GC/[SBCu(II)Gd(III)], GC/MWCNT-COOH and GC/[SBCu(II)Gd(III)]@MWCNT-COOH show the redox characteristics of all three materials (Fig. 10). The oxidation current value obtained for GC/[SBCu(II)Gd(III)], GC/MWCNT-COOH and GC/[SBCu(II)Gd(III)]@MWCNT-COOH are 13, 23.7 and 20.9 μA, respectively. The GC/MWCNT-COOH shows highest oxidation current attributed to their most conducting behavior compared to other materials. The increase in current of GC/[SBCu(II)Gd(III)]@MWCNT-COOH compared to [GC/SBCu(II)Gd(III)]

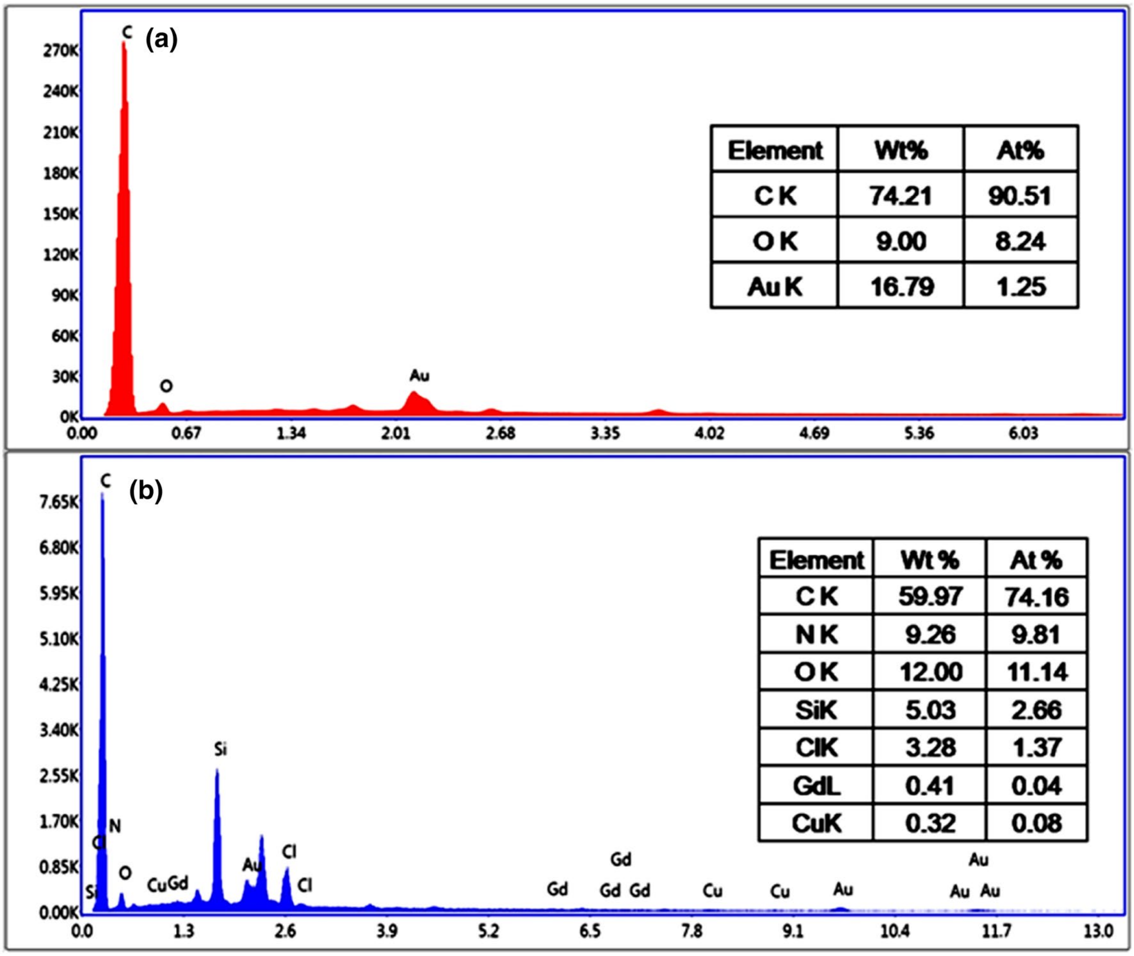

Fig. 7 EDAX spectra of **a** MWCNT-COOH and **b** [SBCu(II)Gd(III)]@MWCNT-COOH

confirmed the successful grafting of [SBCu(II)Gd(III)] with MWCNT-COOH.

3.10.2 Electrochemical impedance measurement

Electrical impedance spectroscopy (EIS) is a frequency dependent technique which uses electronically conducting electrodes for characterizing the electrical properties of materials and their interfaces [58, 59]. Figure 11 shows the Nyquist plots of GC/[SBCu(II)Gd(III)], GC/MWCNT-COOH and GC/[SBCu(II)Gd(III)]@MWCNT-COOH electrodes in 0.1 M KCl containing 2.0 mM $Fe(CN)_6^{3-}/Fe(CN)_6^{4-}$ (1:1 molar ratio) in frequency range: 100 kHz–0.1 Hz and applied potential of 0.2 V. It is observed that Nyquist plots of the materials does not comparise exact semicircular arc (i.e., centres are found below the real Z axis), which is signature of non–Debye type of relaxation [60]. The Nyquist plots were fitted with Randle's equivalent circuit models for quantitative evaluation of resistive and capacitive behavior of electrode. The $(R_s(Q_f(R_f(Q_dR_{ct}))))$ is found most suitable circuit fitted to all three electrodes including parameters: R_s, the solution resistance, an interfacial double layer capacitance related to constant phase element (CPE), here expressed by Q, charge transfer reaction as well as diffusion of ions (from electrolyte to interface) responsible for occurrence of charge transfer resistance (R_{ct}), Q_d related to non-ideal double layer capacity and surface film features expressed by Q_f and R_f [61]. The parameters of best fit Randle's equivalent circuit $(R_s(Q_f(R_f(Q_dR_{ct}))))$ are summarized in Table 4. The R_{ct} values observed for GC/[SBCu(II)Gd(III)], GC/MWCNT-COOH and GC/[SBCu(II)Gd(III)]@MWCNT-COOH are 2.021×10^{14}, 1.895×10^{5} and 3.379×10^{9} Ω, respectively. The lowest R_{ct} value for GC/MWCNT-COOH referred to its most conducting behavior among three materials while the R_{ct} value is highest for GC/[SBCu(II)Gd(III)] due to the highest resistive or least conducting nature of heteronuclear bimetallic Schiff base complex, [SBCu(II)Gd(III)]. The R_{ct} value of GC/[SBCu(II)Gd(III)]@ MWCNT-COOH is intermediate of above two materials, i.e., on successful

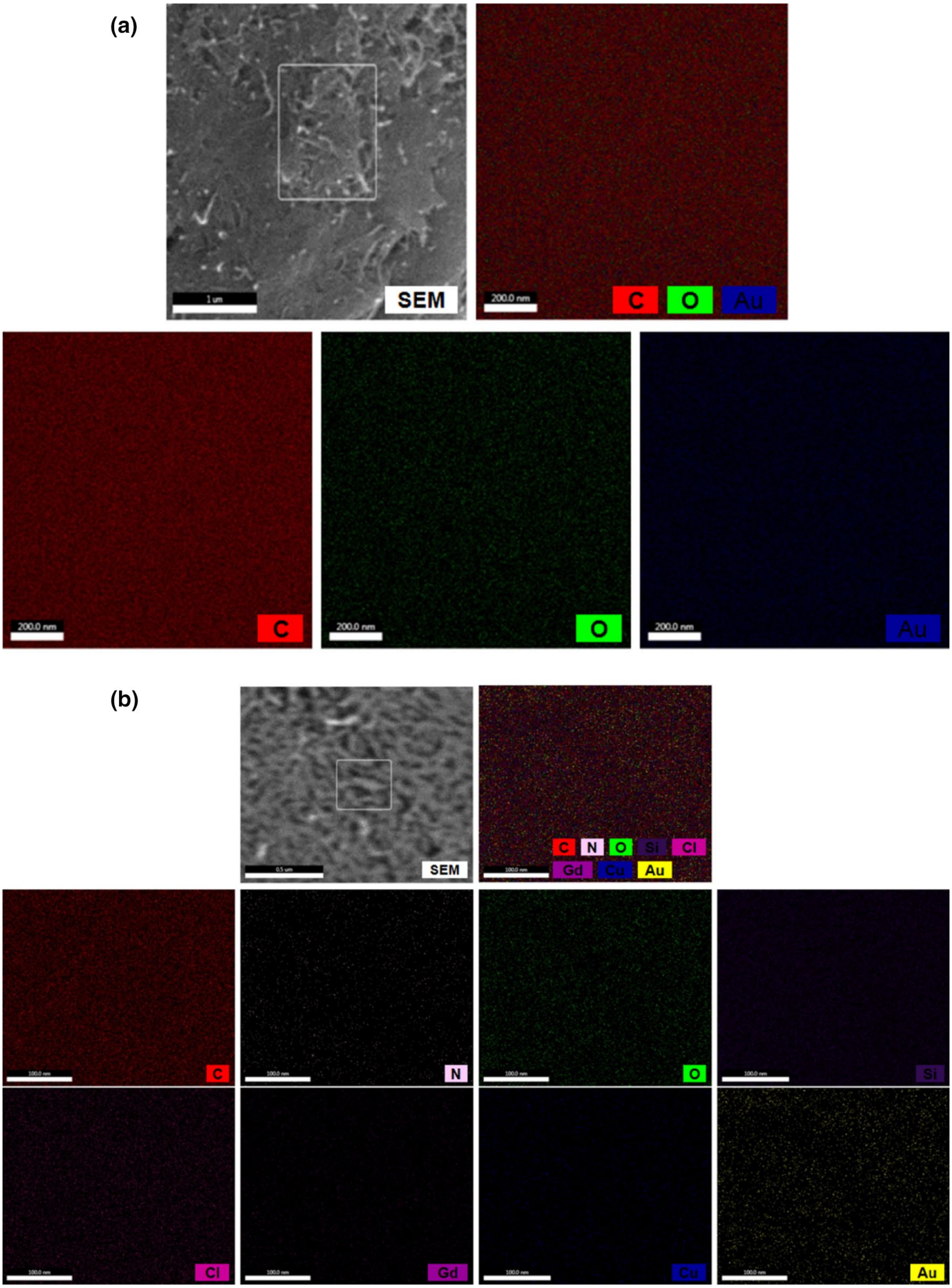

Fig. 8 **a** Elemental mapping for MWCNT-COOH. **b** Elemental mapping for [SBCu(II)Gd(III)]@MWCNT-COOH

grafting of [SBCu(II)Gd(III)] to MWCNT-COOH, the conductivity of GC/[SBCu(II)Gd(III)]@MWCNT-COOH is increased compared to the bimetallic complex due to conducting nature of MWCNT-COOH. This result is in good agreement with the results obtained by cyclic voltammetry.

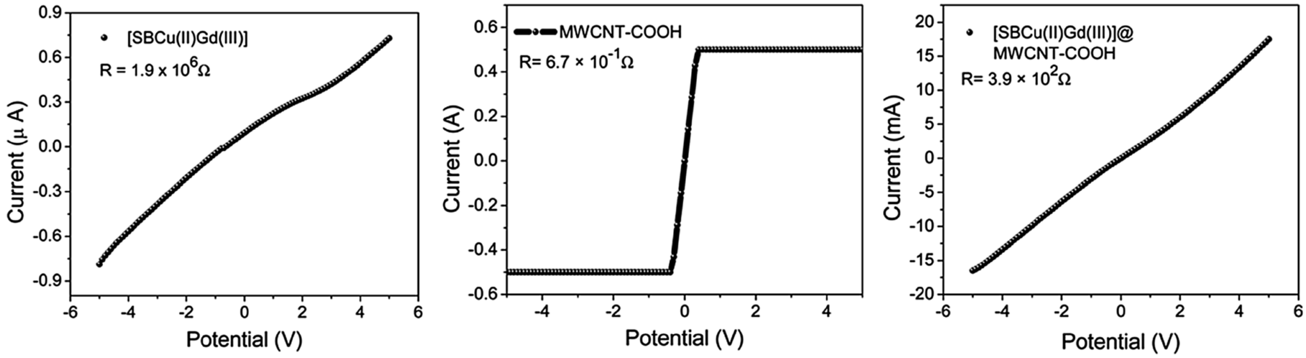

Fig. 9 Current versus Voltage (I–V) curves for [SBCu(II)Gd(III)], MWCNT-COOH and [SBCu(II)Gd(III)]@MWCNT-COOH

Table 3 Slope, flat-band potential (V_{fb}), dielectric constant (ε), resistance and conductivity for GC/[SBCu(II)Gd(III)], GC/MWCNT-COOH and GC/[SBCu(II)Gd(III)]@MWCNT-COOH

Material	Slope	Flat-band potential (V_{fb})	Dielectric constant (ε)	Resistance (Ω)	Conductivity (Sm^{-1})
GC/[SBCu(II)Gd(III)]	5.405	−0.764	$2.608\times10^{19}/N_D$	1.9×10^{6}	5.76×10^{-6}
GC/MWCNT-COOH	11381	−0.453	$1.238\times10^{16}/N_D$	6.7×10^{-1}	6.08×10^{1}
GC/[SBCu(II)Gd(III)]@ MWCNT-COOH	5370	−0.578	$2.625\times10^{16}/N_D$	3.9×10^{2}	2.1×10^{-2}

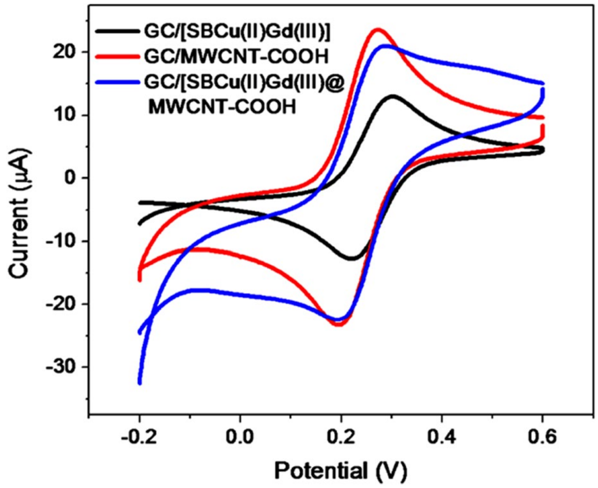

Fig. 10 Cyclic voltammograms of GC/[SBCu(II)Gd(III)], GC/MWCNT-COOH and GC/[SBCu(II)Gd(III)]@MWCNT-COOH electrodes in 2.0 mM $Fe(CN)_6^{3-}/Fe(CN)_6^{4-}$ (1:1 molar ratio) containing 0.1 M KCl

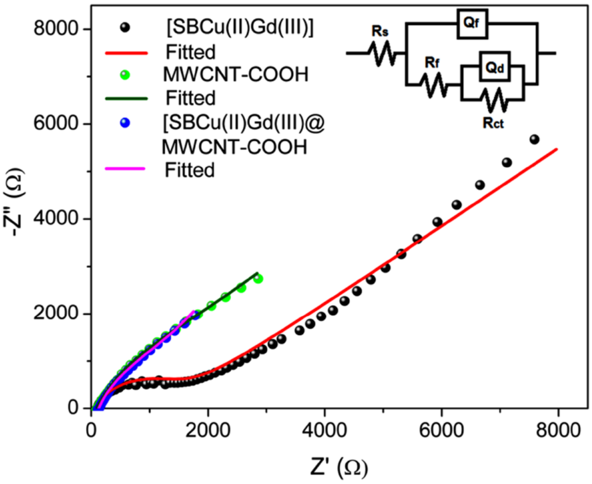

Fig. 11 Nyquist impedance plots along with fitted curve for GC/[SBCu(II)Gd(III)], GC/MWCNT-COOH and GC/[SBCu(II)Gd(III)]@MWCNT-COOH electrodes in 0.1 M KCl containing 2.0 mM $Fe(CN)_6^{3-}/Fe(CN)_6^{4-}$ (1:1 molar ratio). Frequency range: 100 kHz–0.1 Hz, and applied potential: 0.2 V. Inset shows most suitable Randle's equivalent circuit, ($R_s(Q_f(R_f(Q_dR_{ct})))$) corresponds to the Nyquist diagrams

In order to investigate the capacitance and dielectric behavior of GC/[SBCu(II)Gd(III)], GC/MWCNT-COOH and GC/[SBCu(II)Gd(III)]@MWCNT-COOH, the capacitance can be equated from measured total impedance (Z), the real (Z') and imaginary component (Z'') with the corresponding value of the equivalent circuit representing the cell as given below [62],

$$C'(\omega) = \frac{-Z''(\omega)}{\left\{\omega|\,Z(\omega)|^2\right\}}$$

Table 4 Impedance parameter values for GC/[SBCu(II)Gd(III)], GC/MWCNT-COOH and GC/[SBCu(II)Gd(III)]@MWCNT-COOH

Parameter	GC/[SBCu(II)Gd(III)]	GC/MWCNT-COOH	GC/[SBCu(II)Gd(III)]@MWCNT-COOH
R_s (Ω)	98.69	125.8	100.6
Q_f	1.138×10^{-6}	2.802×10^{-4}	1.626×10^{-4}
n_1	0.8	0.8	0.8
R_f (Ω)	1339	3728	3903
Q_d	1.331×10^{-4}	4.642×10^{-4}	3.185×10^{-4}
n_2	0.4	0.8	0.6
R_{ct} (Ω)	2.021×10^{14}	1.895×10^{5}	3.379×10^{9}

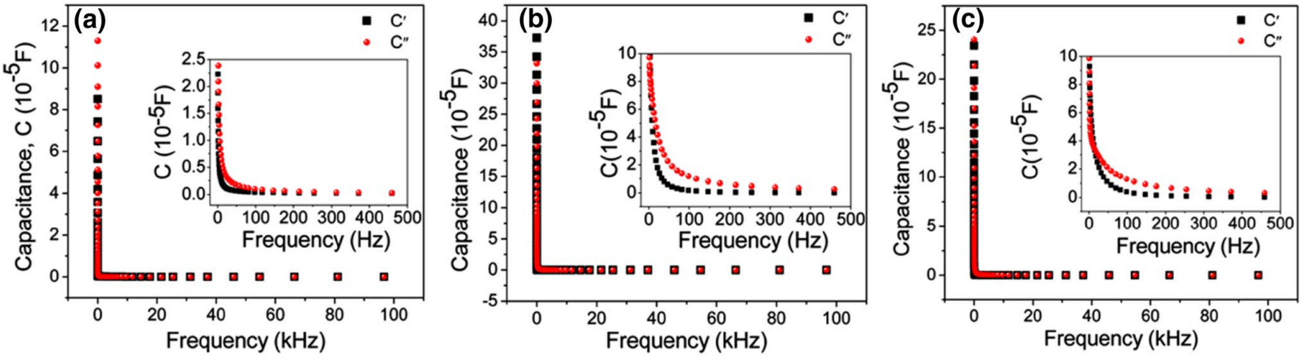

Fig. 12 Frequency dependent capacitive behavior of **a** GC/[SBCu(II)Gd(III)], **b** GC/MWCNT-COOH and **c** GC/[SBCu(II)Gd(III)]@MWCNT-COOH

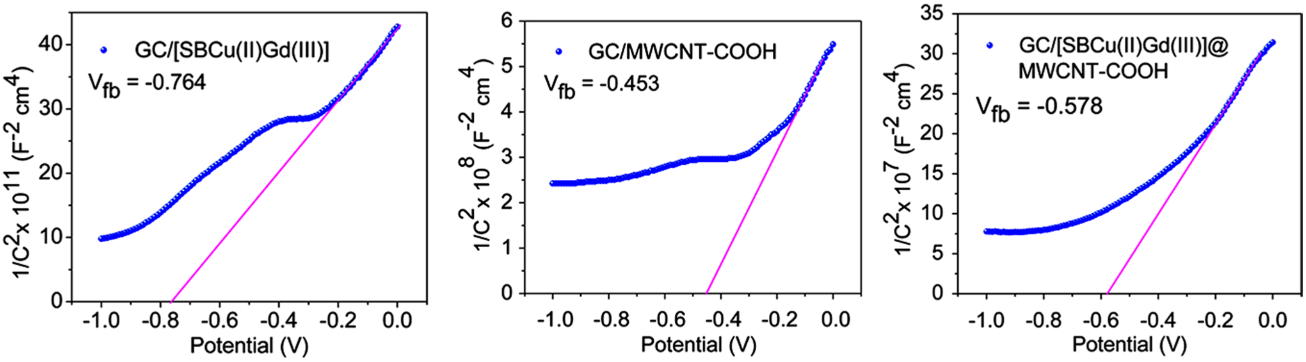

Fig. 13 The capacitance of the GC/[SBCu(II)Gd(III)], GC/MWCNT-COOH and GC/[SBCu(II)Gd(III)]@MWCNT-COOH electrodes as a function of applied potential (Mott–Schottky plots)

$$C''(\omega) = \frac{Z'(\omega)}{\left\{\omega|Z(\omega)|^2\right\}}$$

where, ω is the angular frequency of the a.c. signal ($\omega = 2\pi f$, f being in Hz). At each applied potential, impedance measurement was made in the full frequency range (0.00 Hz–100 kHz) and are shown in Fig. 12. In all three cases of GC/[SBCu(II)Gd(III)], GC/MWCNT-COOH and GC/[SBCu(II)Gd(III)]@MWCNT-COOH, initially capacitance decreases sharply with increase of the frequency, however at around 200 Hz frequency it becomes saturated as at higher applied frequency (> 200 Hz), the charge carriers are unable to respond to the applied AC wave signals.

Hence, the capacitance (C) was determined at frequency 100 Hz at different applied potentials (V) in the range of low current; $1/C^2$ was plotted against V (Mott–Schottky plot), as shown in Fig. 13. From the linear portion of the curves, slope and intercept at potential axis were determined, which revealed the values of dielectric constant and flat-band potential for the materials. A solution of 0.1 M KCl containing 2 mM $Fe(CN)_6^{3-}/Fe(CN)_6^{4-}$ (1:1 molar ratio) was used as the electrolyte solution. The capacitance showed an exponential increase with the increasing voltage. Since the plots are non-linear, their extrapolation was somewhat uncertain, nevertheless, the best possible linear portions of the curves were extrapolated, and intercepts at the potential axis were obtained. The curves show a positive slope indicating n-type semiconductor characteristics of the materials [62]. Further, equating the slope with $1.41 \times 10^{20}/\varepsilon N_D$ [63], ε (dielectric constant) was obtained for a reference donor density, N_D of the materials. The values of slope, flat-band potential (V_{fb}) and dielectric constant (ε) thus obtained are given in Table 3. The slopes for GC/[SBCu(II)Gd(III)], GC/MWCNT-COOH and GC/[SBCu(II)Gd(III)]@MWCNT-COOH were found to be 5.405, 11381 and 5370, respectively with corresponding flat-band potential of −0.764, −0.453 and −0.578 V, respectively. The lower slope for GC/[SBCu(II)Gd(III)] signified the strong dielectric behavior of the material. However the slope for nano hybrid material, GC/[SBCu(II)Gd(III)]@MWCNT-COOH was in-between that of GC/MWCNT-COOH and GC/[SBCu(II)Gd(III)] indicating that on anchoring of [SBCu(II)Gd(III)] over MWCNT-COOH, the dielectric property of material becomes weaker and therefore, increased conductivity is obtained. Further, one can also observe a positive shift in the flat-band potential for hybrid material as compared to GC/[SBCu(II)Gd(III)], which shows more conducting nature of GC/[SBCu(II)Gd(III)]@MWCNT-COOH [62]. Additionally, as the donor density is related to conductivity as $\sigma = en\mu$, where e is the electronic charge, n is carriers concentration, μ is mobility and σ is the electrical conductivity of material [64], the maximum charge carriers concentration is expected for GC/MWCNT-COOH. The similar trend in the conducting properties of these materials was revealed by CV, EIS, and DC electrical conductivity studies.

3.11 Optical and electrochemical band-gaps

The UV–Vis spectra of [SBCu(II)Gd(III)], MWCNT-COOH and [SBCu(II)Gd(III)]@MWCNT-COOH in MeOH and DMF solutions and in solid state (Nujol mull) were used for determination of optical band-gap (Fig. 2c–e). Broad absorption dispersed in entire region of wavelength with no clear appearance of peaks were observed for MWCNT-COOH and [SBCu(II)Gd(III)]@MWCNT-COOH, and hence the optical band-gap (E_g^{opt}) by using onset of absorption edge couldn't be obtained and hence evaluated by using Tuac's relation given below [65],

$$(\alpha h\nu)^n = A\left(h\nu - E_g\right)$$

where α is absorption coefficient (cm^{-1}), $h\nu$ is photon energy, E_g is optical band-gap, A is constant and n depends on the type of electronic transition being equal to 2 or ½ for direct and indirect allowed transition, respectively. By putting the desired values in the above equation, the band-gap (E_g) of the materials was obtained by extrapolating the linear portion of [$(\alpha h\nu)^{1/2}$ vs. $h\nu$] or [$(\alpha h\nu)^2$ vs. $h\nu$] plot to $\alpha \rightarrow 0$ for indirect and direct transitions, respectively. It was observed that the $(\alpha h\nu)^2$ versus $h\nu$ plot retained better linearity in case of all three materials [66] and hence, the E_g^{opt} value was obtained using this plot.

The UV–Vis spectra were recorded in MeOH and DMF solution in order to notice the solvent polarity effect (solvatochromism) on occurrence of absorption peaks. It was observed that in case of more polar solvent (MeOH), because of its low Lewis basicity, the absorption peaks got blue shifted that resulted in higher value of band-gap as compared to that obtained in DMF [46]. The E_g^{opt} values obtained for [SBCu(II)Gd(III)], MWCNT-COOH and [SBCu(II)Gd(III)]@MWCNT-COOH in MeOH were 4.40, 2.72 and 4.12 eV, respectively (Fig. 14a–c) while in DMF corresponding band-gaps were 2.98, 2.47 and 2.70 eV (Fig. 14d–f), respectively (Table 5). The absorption spectra of the materials in solid state was found to be significantly modified compared to that in solution, It was red shifted and hence the optical band-gap decreased in solid state compared to solution. Further, direction of shift depends on the strength of interaction and aggregation; if strong, it's a red shift, otherwise a blue shift and hence the red shift is indicative of an increased intermolecular interactions [47]. The E_g^{opt} values obtained from solid state UV–Vis spectra of [SBCu(II)Gd(III)], MWCNT-COOH and [SBCu(II)Gd(III)]@MWCNT-COOH were 2.49, 1.06 and 1.60 eV, respectively (Fig. 14g–i). However, from spectra in solution and solid state the observed optical band-gap followed the order MWCNT-COOH < [SBCu(II)Gd(III)]@MWCNT-COOH < [SBCu(II)Gd(III)]. The lowest E_g^{opt} of MWCNT-COOH was attributed to their most conducting nature, while highest value for [SBCu(II)Gd(III)] represented its least conducting behavior. For [SBCu(II)Gd(III)]@MWCNT-COOH, the E_g^{opt} value is intermediate of other two materials suggesting that on anchoring of [SBCu(II)Gd(III)] to MWCNT-COOH, resulted in increase of conductivity of material.

Alternatively, the electrochemical band-gap (E_g^{CV}) of materials were obtained by estimation of frontier orbitals (HOMO and LUMO levels) from cyclic voltammetry

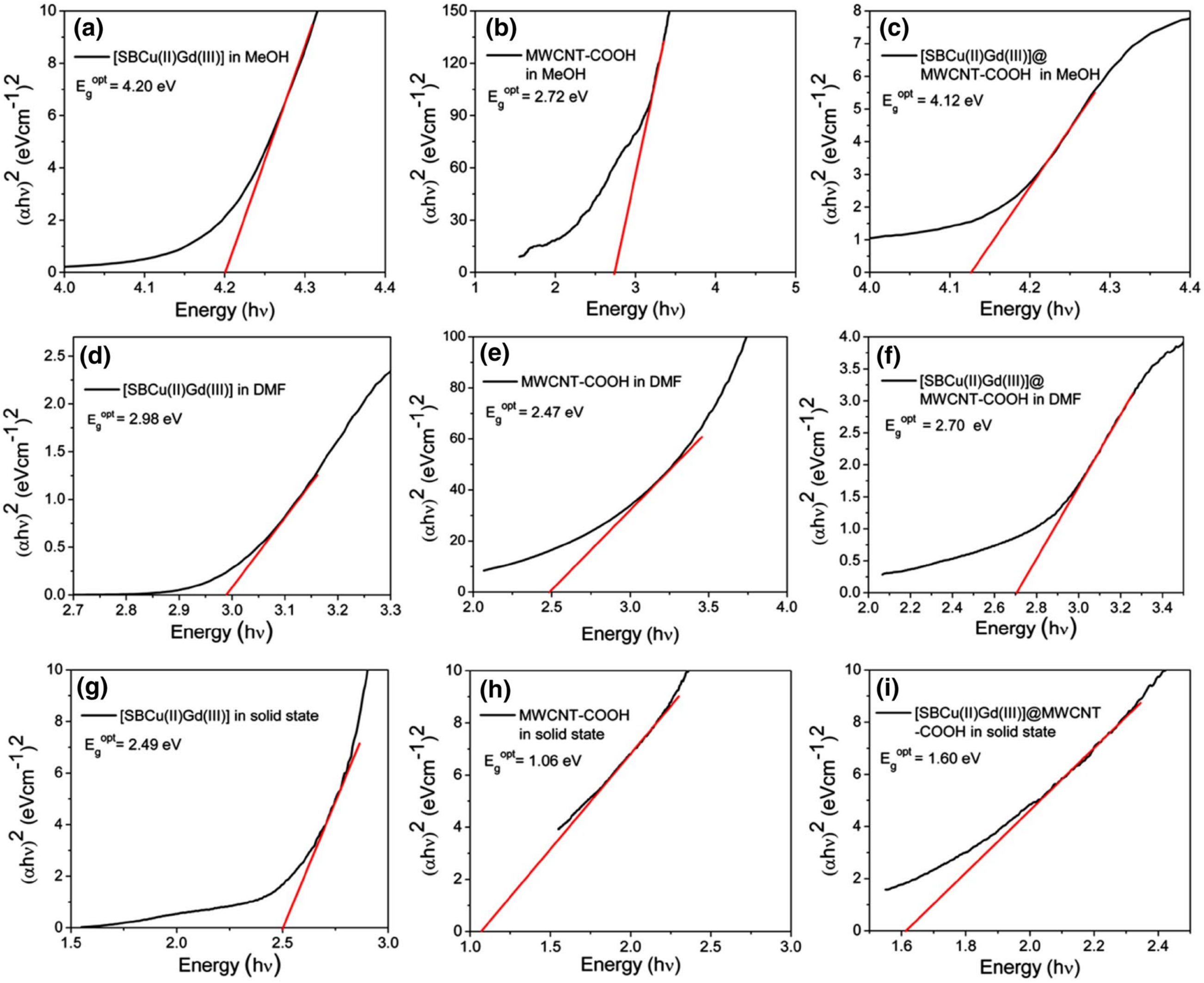

Fig. 14 Optical band gap for [SBCu(II)Gd(III)], MWCNT-COOH and [SBCu(II)Gd(III)]@MWCNT-COOH in MeOH, DMF solution and in solid state (Tuac's plots)

Table 5 Band-gap for materials as obtained from UV–Vis absorption and electrochemical studies

Materials	$E_g^{opt}$$_{/MeOH}$ (eV)	$E_g^{opt}$$_{/DMF}$ (eV)	$E_g^{opt}$$_{/solid\ state}$ (eV)	E_g^{CV} (eV)
[SBCu(II)Gd(III)]	4.20	2.98	2.49	1.14
MWCNT-COOH	2.72	2.47	1.06	–
[SBCu(II)Gd(III)]@ MWCNT-COOH	4.12	2.70	1.60	–

(CV) by using conventional three-electrode cell consisting of glassy carbon (GC) as working electrode, non-aqueous Ag/AgCl electrode as a reference electrode and Pt wire as a counter electrode. Tetrabutylammonium perchlorate (0.1 M in anhydrous dichloromethane) was used as the supporting electrolyte. CV was carried out by drop coating of 0.1 wt% suspension/solution of materials in 1 mL absolute DMF to the GC electrode at a scan rate of 10 mVs^{-1}. The reference electrode was calibrated with ferrocene/ferrocenium (Fc/Fc$^+$) redox couple (with an absolute energy level of – 4.80 eV with respect to vacuum) after each scan. The electrochemical cell was purged with pure nitrogen

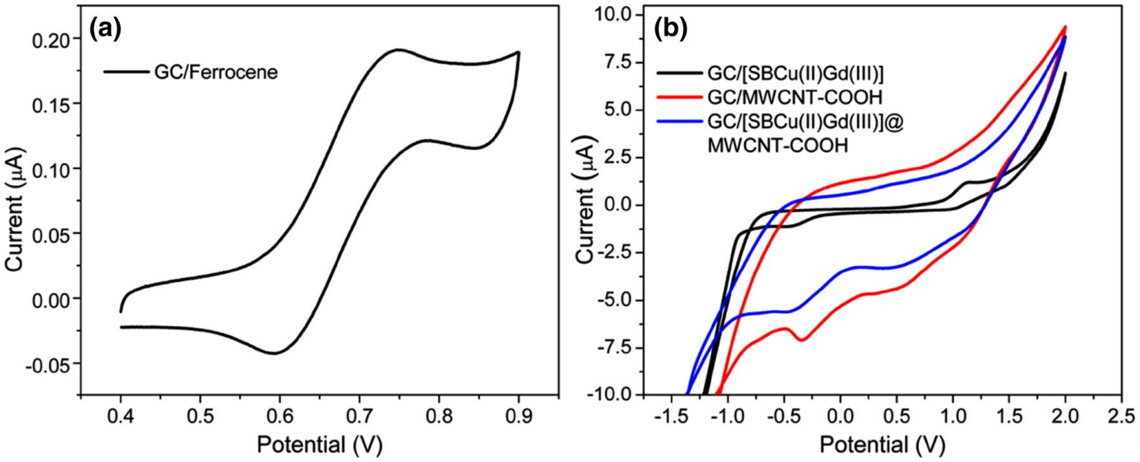

Fig. 15 Cyclic voltammograms of **a** GC/ferrocene and **b** GC/[SBCu(II)Gd(III)], GC/MWCNT-COOH and GC/[SBCu(II)Gd(III)]@MWCNT-COOH in 0.1 M solution of tetrabutylammonium perchlorate in anhydrous dichloromethane

gas for 15 min to remove moisture and diluted gases from cell before starting of the experiment. The HOMO and LUMO levels were calculated from redox onset potential of CV plot by using equations [47]:

$$\mathrm{E_{HOMO}} = -\left(\mathrm{E_{ox}^{onset}} - \mathrm{E_{1/2,\ Fc/Fc^{+}}}\right) - 4.80\ eV$$

$$\mathrm{E_{LUMO}} = -\left(\mathrm{E_{red}^{onset}} - \mathrm{E_{1/2,\ Fc/Fc^{+}}}\right) - 4.80\ eV$$

$$\text{Electrochemical band gap } \left(E_g^{CV}\right) = \left(\mathrm{E_{LUMO}} - \mathrm{E_{HOMO}}\right) eV$$

where, $\mathrm{E_{Fc/Fc^{+}}}$ is the half-wave potential of the ferrocene/ferrocenium (Fc/Fc^{+}) redox couple being obtained as, $\left(E_{1/2,\ Fc/Fc^{+}}\right) = \left(\mathrm{E_{anodic\ peak\ potential}} + \mathrm{E_{anodic\ peak\ potential}}\right)/2.$

The anodic and cathodic peak potentials for Fc/Fc^{+} redox couple were found to be 0.750 and 0.590 V, respectively giving half-wave potential of the ferrocene/ferrocenium ($\mathrm{E_{1/2,Fc/Fc^{+}}}$) as 0.67 V. For [SBCu(II)Gd(III)], $\mathrm{E_{ox}^{onset}}$ and $\mathrm{E_{red}^{onset}}$ were found to be 0.99 and − 0.15 *V* respectively (Fig. 15) and hence HOMO and LUMO energies were − 5.12 and − 3.98 eV, respectively. The electrochemical band-gap was found to be 1.14 eV (Table 5), which is smaller as compared to optical band-gap (2.49 eV) obtained in the solid state [47]. Further, in case of [SBCu(II)Gd(III)]@ MWCNT-COOH, no oxidation peak was observed, this may be due to low loading of [SBCu(II)Gd(III)] on MWCNT-COOH surfaces. Only reduction peak was observed for MWCNT-COOH, due to reduction of oxygen of –COOH group of MWCNTs. Hence, the electrochemical band-gap for [SBCu(II) Gd(III)]@MWCNT-COOH and MWCNT-COOH could not be obtained by using CV.

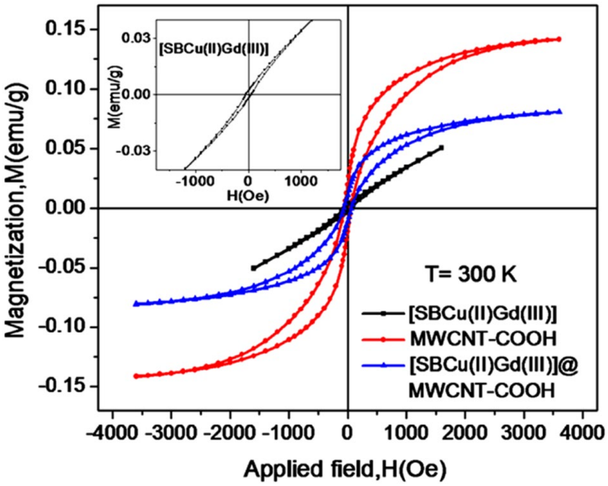

Fig. 16 Magnetic properties: M versus H (Hysteresis) plot for [SBCu(II)Gd(III)], MWCNT-COOH and [SBCu(II)Gd(III)]@MWCNT-COOH. The inset shows hysteresis characteristic of [SBCu(II)Gd(III)]

3.12 Magnetic properties

The magnetic behavior of MWCNT-COOH, [SBCu(II) Gd(III)] and [SBCu(II)Gd(III)]@MWCNT-COOH was studied by VSM and SQUID magnetic measurements. Figure 16 shows the magnetization versus field plot in the range − 4000 to +4000 Oe at room temperature (300 K). The ferromagnetic nature of MWCNT-COOH is due to residual magnetic catalyst (mainly iron) captured during synthesis of MWCNTs by CCVD method [19] which remains sheathed by several graphene sheets of MWCNTs. The values of

Table 6 Magnetic data for [SBCu(II)Gd(III)], MWCNT-COOH and [SBCu(II)Gd(III)]@MWCNT-COOH at 300 K

Materials	Coericivity (Oe)	Remanent magnetization, M_r (emu/g)	Saturation magnetization, M_s (emu/g)
[SBCu(II)Gd(III)]	48.52	0.00209	0.0505
MWCNT-COOH	59.09	0.0196	0.1416
[SBCu(II)Gd(III)]@MWCNT-COOH	64.64	0.0114	0.0804

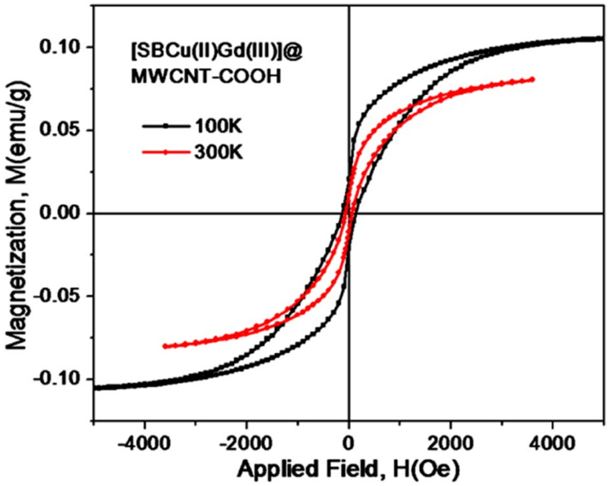

Fig. 17 M versus H (Hysteresis) plot for [SBCu(II)Gd(III)]@MWCNT-COOH at temperature 100 and 300 K

coercivity (H_c), remanent magnetization (M_r) and saturation magnetization (M_s) for MWCNT-COOH were found 59.09 Oe, 0.0196 and 0.1416 emu/g (Table 6), respectively. The complex [SBCu(II)Gd(III)] showed magnetic characteristic due to spin interaction between Cu and Gd metal centers. The values of $H_{c,}$ M_r and M_s for [SBCu(II)Gd(III)] are 48.52 Oe, 0.00209 and 0.0505 emu/g, respectively. On covalent grafting of [SBCu(II)Gd(III)] to MWCNTs surfaces the values of M_r and M_s were found to be 0.0114 and 0.0804 emu/g, respectively, which lie between that of MWCNT-COOH and [SBCu(II)Gd(III)]. This is due to partial dissolution of the residual metal catalyst in the MWCNT-COOH during workup procedure [67]. On the other hand, higher remanent and saturation magnetization of [SBCu(II)Gd(III)]@MWCNT-COOH compared to [SBCu(II)Gd(III)] are due to generation of multinuclear metal centers on the surface of MWCNTs. The values of M_s for these materials are much lower compared to bulk ferromagnetic characteristics of iron. This inconsistency may be because of spin canting effect caused by randomization of iron nanoparticles in between the tubes. The coercivity (64.64 Oe) for [SBCu(II)Gd(III)]@MWCNT-COOH is higher than that of MWCNT-COOH (59.09 Oe). This is attributed to extended organic functionalization on MWCNTs surface. The higher H_c value of [SBCu(II)Gd(III)]@MWCNT-COOH makes it suitable candidate for fabrication of magnetic storage devices [9]. It is observed that the Hc value of [SBCu(II)Gd(III)]@MWCNT-COOH is relatively much higher as compared to the its M_s and M_r values which indicated the weak but irreversible ferromagnetism characteristic of material [68]. As shown in Fig. 17 and Table 7, the H_c value of [SBCu(II)Gd(III)]@MWCNT-COOH is decreasing from 140.43 to 64.64 Oe as temperature increases from 100 to 300 K, this is due to anisotropic nature of Fe nanoparticles encapsulated in the MWCNTs [20]. At higher temperature, the alignment of domains get disturbed due to thermal motion of electrons, which may be cause of decrease in coercivity value with increase in temperature [15]. Furthermore, Fig. 18a shows the temperature dependent magnetization of [SBCu(II)Gd(III)]@MWCNT-COOH at 15000 Oe. Zero field cooled (ZFC) and field cooled (FC) measurements were performed in the temperature 2–300 K. It is noted that the FC and ZFC plots are overlapping with each other in the entire temperature region. This confirmed the single magnetic phase nature of material. Hence no secondary phase is responsible for this ferromagnetism indicating the weak but quite irreversible ferromagnetic nature of [SBCu(II)Gd(III)]@MWCNT-COOH [68]. To understand the type of exchange interaction of domains in [SBCu(II)Gd(III)]@MWCNT-COOH, the linear portion of the χ^{-1} versus T plot (Fig. 18b) was fitted to Curie–Weiss law at two different slopes with intercept in both higher and lower temperature regions. The intercept at high temperature region shows the strong antiferromagnetic nature of domains while intercept at low temperature is signature of weak antiferromagnetism exchange interaction of domains.

Table 7 Variation in H_c, M_r and M_s values of [SBCu(II)Gd(III)]@MWCNT-COOH with Temperature

Temperature (K)	Coericivity, H_c (Oe)	Remanent magnetization, M_r (emu/g)	Saturation magnetization, M_s (emu/g)
100	140.43	0.0201	0.1052
300	64.64	0.0114	0.0804

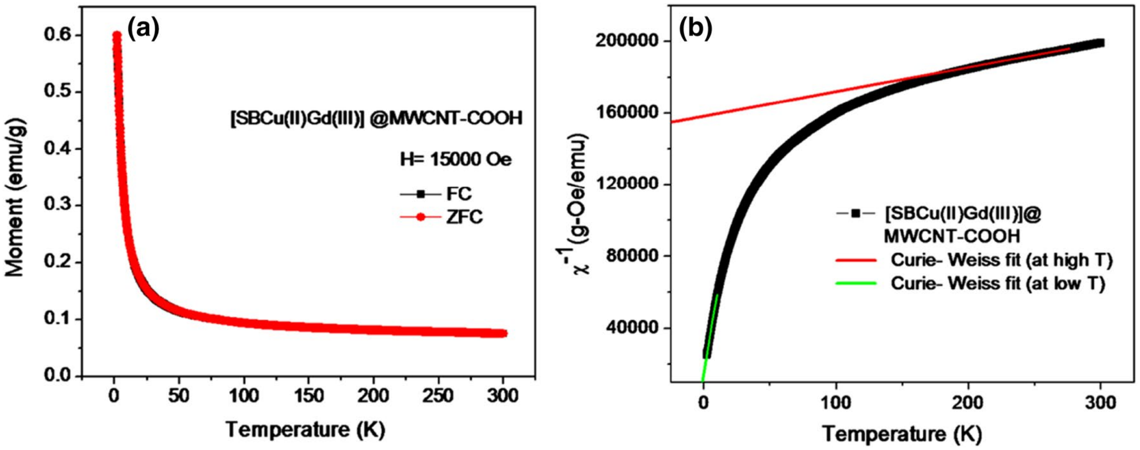

Fig. 18 a Temperature dependent magnetization (FC and ZFC) and **b** Temperature dependent inverse magnetic susceptibility plot for [SBCu(II) Gd(III)]@MWCNT-COOH

4 Conclusions

We have utilized the carboxylic acid functionality of mutiwalled CNTs for their further functionalization with a Cu(II)–Gd(III) heteronuclear bimetallic Schiff base complex for the synthesis of a nano-inorganic hybrid magnetic material. The successful functionalization of MWCNT-COOH with Cu(II)–Gd(III) heteronuclear bimetallic Schiff base complex is confirmed by combination of spectroscopic and surface analysis like FTIR, UV–Vis, powder XRD, Raman, TGA, TEM, HRSEM, EDAX and elemental mapping. After incorporation of heteronuclear bimetallic Schiff base complex, [SBCu(II)Gd(III)] to MWCNT-COOH, the crystalline and tubular structure of the MWCNTs remains essentially unchanged as confirmed by powder XRD studies. The complex [SBCu(II) Gd(III)] showing feeble conductivity changes into better conducting material [SBCu(II)Gd(III)]@MWCNT-COOH with higher value of oxidation current and electrical conductivity after grafting to MWCNT-COOH. The $(R_s(Q_f(R_f(Q_dR_{ct}))))$ is the best fitted circuit for all three materials and shows well agreement with the result obtained by cyclic voltammetry and DC electrical conductivity. The Mott–Schottky analysis suggested n-type semiconductor characteristics of the materials and stronger dielectric behavior of [SBCu(II)Gd(III)] compared to [SBCu(II)Gd(III)]@MWCNT-COOH. The trend of optical band gap is found to be MWCNT-COOH < [SBCu(II) Gd(III)]@MWCNT-COOH < [SBCu(II)Gd(III)] suggested increased conductivity of [SBCu(II)Gd(III)]@MWCNT-COOH compared to [SBCu(II)Gd(III)]. The newly synthesized nano-inorganic hybrid material, [SBCu(II)Gd(III)]@ MWCNT-COOH exhibited typical ferromagnetic characteristics at room temperature. The Field and temperature dependent magnetization trends show weak but quite irreversible ferromagnetic nature of [SBCu(II)Gd(III)]@ MWCNT-COOH.

Acknowledgements We are thankful to DST Nano mission, New Delhi, India for financial support (Project No. SR/NM/NS-1212/2013) to undertake present research work and providing VSM facility. We are grateful to Prof. O. N. Srivastava and Prof. R. K. Singh, Department of Physics, Institute of Science, Banaras Hindu University for providing TEM and hydraulic pressure equipment facility (for making pellets), respectively. We are thankful to Central Instrument Facility, IIT (BHU*)*, Varanasi for HRSEM, EDAX and SQUID studies. Electrochemical Impedance facility provided by Dr. V. Ganesan, Department of Chemistry, Institute of Science, Banaras Hindu University is gratefully acknowledged. We are also thankful to Dr. Pankaj Srivastava, Department of Chemistry, Institute of Science, Banaras Hindu University for their valuable discussion on capacitive and dielectric studies of materials.

References

1. K.S. Ibrahim, Carbon Lett. **14**, 131–144 (2013)
2. M.S. Si, D.S. Xue, Appl. Phys. Lett. **92**, 081907 (2008)
3. A. Lekawa-Raus, J. Patmore, L. Kurzepa, J. Bulmer, K. Koziol, Adv. Funct. Mater. **24**, 3661–3682 (2014)
4. C. Berger, Y. Yi, Z.L. Wang, W.A. de Heer, Appl. Phys. A **74**, 363–365 (2002)
5. W. Khan, R. Sharma, P. Saini, in *Carbon Nanotubes—Current Progress of Their Polymer Composites*, ed. by M.R. Berber, I.H. Hafez (Intech Open, Rijeka, 2016), pp. 1–45
6. P.-C. Ma, M.-Y. Liu, H. Zhang, S.-Q. Wang, R. Wang, K. Wang, Y.-K. Wong, B.-Z. Tang, S.-H. Hong, K.-W. Paik, J.-K. Kim, ACS Appl. Mater. Interfaces **1**(5), 1090–1096 (2009)
7. Y. Yusof, M.I. Zaidi, M.R. Johan, J. Nanomater. **2016**, 6141496 (2016)
8. H.A. Alturaif, Z.A. ALOthman, J.G. Shapter, S.M. Wabaidur, Molecules **19**, 17329–17344 (2014)
9. A. Hariharasubramanian, Y.D. Ravichandran, R. Rajesh, R. Rajkumari, G.K. Selvan, S. Arumugam, Fuller. Nanot. Carbon Nanostruct. **22**, 874–886 (2014)
10. K. Balasubramanian, M. Burghard, Small **1**, 1180–1192 (2005)

11. KFu Ya-Ping Sun, Y. Lin, W. Huang, Acc. Chem. Res. **35**, 1096–1104 (2002)
12. M. Samadishadlou, M. Farshbaf, N. Annabi, T. Kavetskyy, R. Khalilov, S. Saghfi, A. Akbarzadeh, S. Mousavi, Artif. Cells Nanomed. Biotechnol. **46**, 1314–1330 (2017)
13. S.K. Park, Q. Mahmood, H.S. Park, Nanoscale **5**, 12304–12309 (2013)
14. E.T. Mickelson, C.B. Huffman, A.G. Rinzler, R.E. Smalley, R.H. Hauge, J.L. Margrave, Chem. Phys. Lett. **296**, 188–194 (1998)
15. J. Chen, A.M. Rao, S. Lyuksyutov, M.E. Itkis, M.A. Hamon, H. Hu, R.W. Cohn, P.C. Eklund, D.T. Colbert, R.E. Smalley, R.C. Haddon, J. Phys. Chem. B **105**, 2525–2528 (2001)
16. T. Ramanathan, F.T. Fisher, R.S. Ruoff, L.C. Brinson, Chem. Mater. **17**, 1290–1295 (2005)
17. P. Kar, A. Choudhury, Sensor Actuators B **183**, 25–33 (2013)
18. G. Prabhavathi, M. Arjun, R. Yamuna, J. Chem. Sci. **129**, 699–706 (2017)
19. R.P. Sahu, A.M. Abdalla, A. Rahman A. Fattah, S. Ghosh, I. K. Puri, in *Advances in Nanomaterials*, ed. by G. Balasubramanian (Springer, Switzerland, 2018), pp. 37–57
20. A.V. Ellis, B. Ingham, J. Magn. Magn. Mater. **302**, 378–381 (2006)
21. K. Kudelska, A. Małolepszy, M. Mazurkiewicz, L. Stobinski, W. Dobrowolski, Acta Phys. Pol. A **119**, 597–599 (2011)
22. A.R.J. Azar, S. Mohebbi, Mater. Chem. Phys. **168**, 85–94 (2015)
23. S.M. Wilkinson, T.M. Sheedy, E.J. New, J. Chem. Educ. **2**, 351–354 (2016)
24. M. Salavati-Niasari, F. Davar, M. Bazarganipour, Dalton Trans. **39**, 7330–7337 (2010)
25. M. Salavati-Niasari, A. Badiei, K. Saberyan, Chem. Eng. J. **173**, 651–658 (2011)
26. M. Salavati-Niasari, E. Esmaeili, H. Seyghalkar, M. Bazarganipour, Inorg. Chim. Acta **375**, 11–19 (2011)
27. R. Rajarao, T.H. Kim, B.R. Bha, J. Coord. Chem. **65**, 2671–2682 (2012)
28. M. Bazarganipour, M. Salavati-Niasari, Appl. Catal. A **502**, 57–64 (2015)
29. M. Bazarganipour, M. Salavati-Niasari, Chem. Eng. J. **286**, 259–265 (2016)
30. H. Veisi, R. Azadbakht, F. Saeidifar, M. Reza Abdi, Catal. Lett. **147**, 976–986 (2017)
31. P.K. Sonkar, V. Ganesan, S.A. John, D.K. Yadav, R. Gupta, RSC Adv. **6**, 107094–107103 (2016)
32. M. Salavati-Niasari, M. Bazarganipour, Appl. Surf. Sci. **255**, 2963–2970 (2008)
33. M. Salavati-Niasari, M. Bazarganipour, Appl. Surf. Sci. **255**, 7610–7617 (2009)
34. M. Salavati-Niasari, M. Bazarganipour, Transit. Met. Chem. **34**, 605–612 (2009)
35. M. Salavati-Niasari, M. Bazarganipour, J. Mol. Catal. A **278**, 173–180 (2007)
36. J. Zhao, Y. Xie, D. Guan, H. Hua, R. Zhong, Y. Qin, J. Fang, H. Liu, J. Chen, Sci. Rep. **5**, 12544 (2015)
37. A. Masotti, A. Caporali, Int. J. Mol. Sci. **14**, 24619–24642 (2013)
38. A.L. Elias, J.A. Rodriguez-Manzo, M.R. McCartney, D. Golberg, A. Zamudio, S.E. Baltazar, F. Lopez-Urias, E. Munoz-Sandoval, L. Gu, C.C. Tang, D.J. Smith, Y. Bando, H. Terrones, M. Terrones, Nano Lett. **5**, 467–472 (2005)
39. M.C.G. López, F. Moro, A.L. Torre, C.J. Gómez-García, P.D. Brown, J. Slageren, A.N. Khlobystov, Nat. Commun. **2**, 407 (2011)
40. Y. Cao, Fuller. Nanotub. Carbon Nanostruct. **23**, 623–626 (2014)
41. J. Li, L. Qi, H. Li, J. Phys. Chem. C **120**, 22865–22872 (2016)
42. F.Z.C. Fellah, S. Boulefred, A.C. Fellah, B.E. Rez, C. Duhayon, J.P. Sutter, Inorg. Chim. Acta **439**, 24–29 (2016)
43. O.H. Shihab, Al-Obaidi. Bioinorg. Chem. Appl. **2012**, 1–6 (2012)
44. L.J. Singh, R.H. Singh, Int. J. Inorg. Chem. **2013**, 1–9 (2013)
45. P.R. Reddy, A. Shilpa, N. Raju, P. Raghavaiah, J. Inorg. Biochem. **105**, 1603–1612 (2011)
46. F. Kolcu, I. Kaya, RSC Adv. **7**, 8973–8984 (2017)
47. M. Gupta, S.K. Pal, Langmuir **32**, 1120–1126 (2016)
48. A. Bhattacharyya, A. Bauzá, S. Sproules, L.S. Natrajan, A. Fronter, S. Chattopadhyay, Polyhedron **137**, 332–346 (2017)
49. M. Jagadeesh, M. Lavanya, S.K. Kalangi, Y. Sarala, C. Ramachandraiah, A.V. Reddy, Specrtochim. Acta A **135**, 180–184 (2015)
50. P.K. Bhaumik, K. Harms, S. Chattopadhyay, Polyhedron **68**, 346–356 (2014)
51. X. Geng, J. Jing, Y. Cen, R. Datta, J. Liang, J. Nanomater. **2015**, 1–10 (2015)
52. L. Bokobza, J. Zhang, Express. Polym Lett. **6**, 601–608 (2012)
53. O.-K. Park, S. Lee, H.-I. Joh, J.K. Kim, P.-H. Kang, J.H. Lee, B.-C. Ku, Polymer **53**, 2168–2174 (2012)
54. S. Banerjee, S.S. Wong, Nano Lett. **2**, 49–53 (2002)
55. B. Massoumi, V.B. Valizada, M. Jaymand, RSC Adv. **5**, 40840–40848 (2015)
56. T.K. Han, L.B. Fen, N.M. Nee, R. Ahmad, M.R. Johan, Adv. Mat. Res. **194–196**, 618–624 (2011)
57. C.M. White, R. Banks, I. Hamerton, J.F. Watts, Prog. Org. Coat. **90**, 44–53 (2016)
58. I. Hafaiedh, S. Ameur, A. Abdelghani, J. Nanomed. Nanotechnol. **6**, 271–275 (2012)
59. R. Gupta, P.K. Rastogi, V. Ganesan, D.K. Yadav, P.K. Sonkar, Sens Actuators B **239**, 970–978 (2017)
60. K. Parida, S.K. Dehury, R.N.P. Choudhary, Phys. Lett. A **380**, 4083–4091 (2016)
61. H. Xu, S. Liu, L.Y. Guo, Y.J. Li, K.C. Shen, C.S. Guan, W.M. Wang, Int. J. Electrochem. Sci. **10**, 4985–5000 (2015)
62. G.A.M. Ali, M.M. Yusoff, E.R. Shaaban, K.F. Chong, Ceram. Int. **43**, 8440–8448 (2017)
63. I.C. Neetu, S. Maurya, A.K. Singh, P. Gupta, L. Srivastava, Bahadur. Chem. Select **2**, 4267–4276 (2017)
64. E.G. Víllora, K. Shimamura, Y. Yoshikawa, T. Ujiie, K. Aoki, Appl. Phys. Lett. **92**, 202120 (2008)
65. M.M. Rashad, A.M. Hassan, A.M. Nassar, N.M. Ibrahim, A. Mourtada, Appl. Phys. A **117**, 77–890 (2014)
66. Y. Kaya, H. Mutlu, G. Irex, G. U. J. Sci. **23**, 13–18 (2010)
67. G. Gao, Q. Zhang, X.-B. Cheng, J.G. Shapter, T. Yin, R. Sun, D. Cui, Sci. Rep. **5**, 17553 (2015)
68. J. Datta, A. Dey, S.K. Neogi, M. Das, S. Middya, R. Jana, S. Bandyopadhyay, A. Layek, P.P. Ray, IEEE Trans Electron. Devices **64**, 4724–4730 (2017)